OPEN ACCESS Freely available online

PLOS ONE

Molecular and Cellular Features of Murine Craniofacial and Trunk Neural Crest Cells as Stem Cell-Like Cells

Kunie Hagiwara[1,4], Takeshi Obayashi[2], Nobuyuki Sakayori[3], Emiko Yamanishi[3], Ryuhei Hayashi[4], Noriko Osumi[3]*, Toru Nakazawa[1], Kohji Nishida[4]

1 Department of Ophthalmology, Tohoku University Graduate School of Medicine, Seiryo-cho, Aoba-ku, Sendai, Japan, **2** Division of Applied Informatics for Human and Life Science, Tohoku University Graduate School of Information Science, Aramaki-Aza-Aoba, Aoba-ku, Sendai, Japan, **3** Division of Developmental Neuroscience, Tohoku University Graduate School of Medicine, Seiryo-cho, Aoba-ku, Sendai, Japan, **4** Department of Ophthalmology, Osaka University Graduate School of Medicine, Yamadaoka, Suita, Japan

Abstract

The outstanding differentiation capacities and easier access from adult tissues, cells derived from neural crest cells (NCCs) have fascinated scientists in developmental biology and regenerative medicine. Differentiation potentials of NCCs are known to depend on their originating regions. Here, we report differential molecular features between craniofacial (cNCCs) and trunk (tNCCs) NCCs by analyzing transcription profiles and sphere forming assays of NCCs from *P0-Cre/floxed-EGFP* mouse embryos. We identified up-regulation of genes linked to carcinogenesis in cNCCs that were not previously reported to be related to NCCs, which was considered to be, an interesting feature in regard with carcinogenic potentials of NCCs such as melanoma and neuroblastoma. Wnt signal related genes were statistically up-regulated in cNCCs, also suggesting potential involvement of cNCCs in carcinogenesis. We also noticed intense expression of mesenchymal and neuronal markers in cNCCs and tNCCs, respectively. Consistent results were obtained from *in vitro* sphere-forming and differentiation assays. These results were in accordance with previous notion about differential potentials of cNCCs and tNCCs. We thus propose that sorting NCCs from *P0-Cre/floxed-EGFP* mice might be useful for the basic and translational research of NCCs. Furthermore, these newly-identified genes up-regulated in cNCC would provide helpful information on NC-originating tumors, developmental disorders in NCC derivatives, and potential applications of NCCs in regenerative medicine.

Citation: Hagiwara K, Obayashi T, Sakayori N, Yamanishi E, Hayashi R, et al. (2014) Molecular and Cellular Features of Murine Craniofacial and Trunk Neural Crest Cells as Stem Cell-Like Cells. PLoS ONE 9(1): e84072. doi:10.1371/journal.pone.0084072

Editor: Hitoshi Okazawa, Tokyo Medical and Dental University, Japan

Received August 4, 2013; **Accepted** November 11, 2013; **Published** January 20, 2014

Funding: This study was supported by a project for the realization of regenerative medicine from the Ministry of Education, Culture, Sports, Science, and Technology (MEXT) of Japan given to K.N. and by KAKENHI from MEXT to N.O. The funders had no role in study design, data collection and analysis, decision to publish, or preparation of the manuscript.

Competing Interests: The authors have declared that no competing interests exist.

* E-mail: osumi@med.tohoku.ac.jp

Introduction

Neural crest cells (NCCs) are cell populations that originate in the early stage of the vertebrate embryo from the dorsal region of the neural tube. They delaminate from the border of neural and non-neural areas of the ectoderm. After delamination, NCCs vigorously proliferate during migration towards various locations within the embryonic body, and differentiate into a wide range of cell types and tissues, including neurons and glial cells of the peripheral nervous systems (PNS), smooth muscles of the heart and great vessels, bone, cartilage, connective tissue of the face, and melanocytes in the skin.

The migration patterns and differentiation fates of NCCs have been well characterized in avian and rodent embryos [1]. Trunk NCCs (tNCCs) emerge from the trunk region of the neural epithelium, and those migrating just beneath the ectoderm will form pigment cells in the skin and others taking a ventral pathway via the somites will differentiate into neurons and glia of the PNS as well as chromaffin cells in the adrenal gland [2]. Craniofacial NCCs (cNCCs) emerge from the forebrain, midbrain and hindbrain regions of the neural epithelium, and populate the frontonasal area or the pharyngeal arches depending on their original positions [3]. These cNCCs produce not only neurons, glia and melanocytes, but also the majority of the connective and skeletal tissue of the head [1]. Therefore, cNCCs show wider variation in their differentiated cell types than tNCCs during normal development.

Another feature characteristic to NCCs is its relation to tumor formation. Melanoma is a common skin cancer derived from pigment cells of NC-origin [4]. It is also believed that neuroblastoma, one of the most frequent child cancers occurred in the sympathetic nervous systems and adrenal gland, is originated from the NCCs [5]. Another example of a cancer thought to be NC-origin is Ewing sarcoma, an aggressive bone and soft tissue tumors [6]. Considering a recent idea of cancer stem cells [7,8], NCCs may share molecular features common to malignant tumors.

In the present study, we performed transcriptome analyses of cNCCs and tNCCs using genetically engineered mice that specifically label NCCs. We also clarified difference in expression profiles of cNCCs and tNCCs from those of inducible pluriopotent stem cells (iPSCs) and embryonic stem cells (ESCs). Furthermore, we also carried out sphere-forming and differentiation assays to know proliferation and differentiation potentials of cNCCs and tNCCs *in vitro*. Both of approaches consistently revealed differential characters of NCCs as multipotent stem cells, and possibly as

cancer stem cells. These results not only provide useful information for NCC application in regenerative medicine but also contribute to develop specific therapeutics for preventing metastatic cascades of NC-derived tumors.

Materials and Methods

Animals

Transgenic (TG) mice expressing the Cre enzyme induced by the myelin protein zero (P0) promoter [9] were crossed with the *CAG-CAT-EGFP* TG line [10]. In *P0-Cre/floxed-EGFP* double TG (*P0-Cre; EGFP*) mice, NCCs were identified by evaluating the expression of EGFP after *P0-Cre*-mediated DNA recombination [11]. To eliminate pigmentation in the embryonic tissue of double TG lines, mice originally of the C57/BL6J background were crossed with mice of an ICR background (Japan Charles River, Tokyo, Japan) for 5–6 generations as described previously [12]. At mid-day of identifying a vaginal plug was considered as E0.5. P0-Cre recombinase TG mice were kindly provided by Dr. K. Yamamura (Kumamoto University, Kumamoto, Japan). *CAG-CAT-EGFP* TG mice were kindly provided by Dr. J. Miyazaki (Osaka University, Osaka, Japan) and maintained at Tohoku University. All experimental animal procedures described in this study were approved by the Ethics Committee for Animal Experiments of Tohoku University Graduate School of Medicine (#2012-134).

Preparation of cells from mouse embryos

P0-Cre; EGFP embryos were resected into Hanks' balanced salt solution ($HBSS^+$; GIBCO 14025-092) containing 10% fetal bovine serum (FBS; GIBCO 12483) and 1% penicillin/streptomycin (P/S; GIBCO 15140-122). The craniofacial and trunk regions were separated, and heart fields were separated from the trunk region. Each fraction was incubated with 0.25% collagenase (Sigma C5894) in $HBSS^+$ for 30 min at 37°C. After rinsing in PBS, embryonic tissues were incubated in 0.25% trypsin-EDTA for 30 min and then mechanically dissociated in $HBSS^+$ containing FBS. The cells were collected by centrifugation at 800×*g* for 5 min at 4°C.

Flow cytometric analysis and fluorescence-activated cell sorting

For flow cytometry and cell sorting, a FACS Aria II (BD Biosciences, San Diego, CA, USA) was used. Sorted $EGFP^+$ and $EGFP^-$ cells were resuspended in sphere culture medium and cultured in non-adhesive 12-well culture plates (Cell-Seed, Tokyo, Japan CS2018).

RNA microarray analysis

Total RNA was obtained from harvested $EGFP^+$ and $EGFP^-$ cells using an RNeasy plus Micro Kit (Qiagen 74034) and DNase I (Qiagen 79254). Comprehensive gene expression microarray analysis was performed with a 3D-Gene (Toray Industries). Data were analyzed using R language [13]. We also analyzed using Gene Spring (Agilent Technologies, Santa Clara, CA, USA). The microarray data has been submitted to the GEO database (accession No: GSE39191).

Analysis of stem cell gene expression

Stem cell genes with the following GO annotations were selected; "stem cell maintenance" (GO:0019827), "germ-line stem cell maintenance" (GO:0030718), "somatic stem cell maintenance" (GO:0035019), "stem cell differentiation" (GO:0048863), "stem cell development" (GO:0048864), "hemopoietic stem cell differentiation" (GO:0060218). An F-test was applied to evaluate alterations in gene expression of stem cell genes compared with that of all genes on the microarray. Biologically duplicated samples were averaged for the F-test. The Bonferroni multi-test correction was applied to the data.

Clustering analysis

For gene clustering of the microarray analysis, we first selected 347 genes significantly altered in any of the samples under two criteria; an ANOVA FDR p-value of <0.05 and at least a 4-fold expression change. Then, gene clustering was performed using hclust (complete linkage, 1 - Pearson's correlation) and cutree functions in R language [13]. The number of clusters was manually set to seven. Finally, GO enrichment tests were performed for each cluster using BiNGO software [14]. Because the enriched GO terms for each cluster were numerous, we omitted highly redundant GO terms including more than 80% of genes in a more significant GO term.

qRT- PCR analysis

Total RNA was obtained by the same method used for microarray analysis as described above. Reverse transcription was performed with a SuperScript First-Strand® III Synthesis Super Mix for qRT-PCR (11752-250, Invitrogen Carlsbad, NM, USA), according to the manufacturer's instructions. qRT- PCR was performed using an ABI Prism 7900HT Sequence Detection System (Applied Biosystems Inc., Foster City, CA, USA), according to the manufacturer's instructions. Primer pairs and TaqMan® MGB probes were designed with Assay by-Design™ (Applied Biosystems). Results were evaluated using the Student's *t* test.

Immunohistochemistry

Cultured cells and frozen tissue sections were fixed with 4% paraformaldehyde and then stained with the following primary antibodies: anti-Sox10 (N-20; Santa Cruz Biotechnology, Santa Cruz, CA, USA), anti-PDGF receptor α-chain (558774; BD Pharmingen, San Diego, CA, USA), anti-PDGF receptor β-chain (#3169; Cell Signaling Technology, Danvers, MA, USA), anti-GFP (ab13970; Abcam, Cambridge, UK), anti-Ap2α, anti-AP-2β (Cell Signaling Technology), anti-Nanog (AB5731; Millipore, Temecula, CA, USA) anti-Nestin (G-20; Santa Cruz Biotechnology), anti-Oct3/4 (MAB1759; R&D Systems, Minneapolis, MN, USA), anti-PAR4 (3G9H7; Santa Cruz Biotechnology), anti-Sox2 (Y-17; Santa Cruz Biotechnology), anti-alpha smooth muscle actin (ab32575; Abcam), anti-βIII-tubulin (MAB1195; R&D Systems), anti-glial fibrillary acidic protein (MAB360; Chemicon International, Temecula, CA, USA) and anti-GFP (MBL, Nagoya, Japan). After washing with Tris-buffered saline, the sections were stained with Alexa Fluor-488 or Alexa Fluor-568 conjugated secondary antibodies (Invitrogen). All sections were counterstained with Hoechst 33342 (Invitrogen).

Cell culture

Sorted $EGFP^+$ and $EGFP^-$ cells were cultured in DMEM/F-12 (1:1) supplemented with 20 ng/mlL epidermal growth factor (EGF; Sigma-Aldrich), 20 ng/ml basic fibroblast growth factor (bFGF; Invitrogen), B27 supplement (Invitrogen) and 10^3 units/ml leukemia inhibitory factor (LIF; Chemicon) at 37°C with 5% CO_2. LIF was added to prevent differentiation as previously described [12]. Cells were seeded onto non-adhesive 6-well culture plates (Cell-Seed) and cultured for 5–7 DIV. To obtain secondary

spheres, primary spheres were dissociated with 0.05% trypsin 0.53 mM EDTA-4Na (Invitrogen, Carlsbad, NM, USA) into a single-cell suspension and then re-seeded into fresh medium.

Differentiation culture

To induce neurogenic and glial differentiation, EGFP$^+$ and EGFP$^-$ spheres were cultured in sphere culture medium without bFGF, EGF or LIF for 7 DIV on dishes coated with ornithine and laminin. For chondrogenic differentiation, spheres were cultured using a hMSC Differentiation Bulletkit, Chondrogenic (Lonza) according to the manufacturer's instructions, and evaluated by staining with alcian blue (Diagnostic Biosystems, Pleasanton, CA, USA). Smooth muscle differentiation was induced by culture in DMEM/F12 containing 2% FBS and 10 ng/ml transforming growth factor β1 (R&D Systems) for 7 DIV. For quantification of adipocyte differentiation by relative fluorescence units (RFU), excitation of the Adipo Red-stained cells was measured at excitation and emission at 485 and 535 nm, respectively.

Results

Isolation of NCCs from *P0-Cre/Floxed-EGFP* mouse embryos

To elucidate the molecular features of NCCs, we planned to isolate NCCs from mouse embryos that contain genetically labeled NCCs. Wnt1-Cre is widely used among NCC-specific Cre-driver lines [15], but this line shows strong activity of Cre in the midbrain region [16]. Another line, i.e., P0-Cre has been established by utilizing a promoter of a gene encoding Shwann cell-specific P0 protein. The specificity of P0-Cre activity in various mouse tissues, especially craniofacial region, has been well proven by checking lack of expression of Cre mRNA and protein [11,12,17–19] except for a very minor leaky labeling in the mesoderm-derived notochord [9], Therefore, we chose *P0-Cre/Floxed-EGFP* mice to analyze molecular and cellular characters of NCCs.

To isolate cNCC and tNCCs, craniofacial and trunk regions were separately dissected from *P0-Cre/Floxed-EGFP* mouse embryos at embryonic day (E) 9.5, E10.5, E11.5 and E12.5 (Fig. 1A). Cells were dissociated from the both regions and analyzed by flow cytometry to assess the intensity of EGFP. These cells were separated into two populations, P0-EGFP positive (EGFP$^+$) and negative (EGFP$^-$) cells (Fig. 1B). The percentage of EGFP$^+$ cells from the craniofacial region increased with embryonic age, while in the trunk region, the frequency of EGFP$^+$ cells was relatively lower than that in the craniofacial region with its highest ratio at E10.5 (Fig. 1C). Therefore, although we noticed that these EGFP$^+$ cells might contain heterogeneous cell populations, we further analyzed these EGFP$^+$ and EGFP$^-$ cell populations from craniofacial and trunk regions.

Expression of typical NCC markers by quantitative real-time (qRT)-PCR

To evaluate NCC character in EGFP$^+$ cells, we examined expression of several NCC and/or mesenchymal markers by qRT-PCR analysis in EGFP$^+$ and EGFP$^-$ cells from craniofacial and trunk regions in E9.5, E10.5, E11.5 and E12.5 embryos. Frequently used markers of NCCs *Pax7*, *Msx1*, *Barx1*, *snail2* and *PDGFRα* showed higher expression in craniofacial EGFP$^+$ cells (Cp) at all embryonic stages examined (Fig. 2A). As we expected, mesenchymal markers such as *Lhx8* and *Akp2* also showed higher expression in Cp (Fig. 2B). *PDGFRβ*, a well-known marker of pericytes, exhibited the same tendency (Fig. 2B). We noticed strong expression of these genes in Cp from E12.5 embryos, while other NCC markers such as *FoxD3 and Sox10* showed remarkably higher expression in trunk EGFP$^+$ cells (Tp) than in Cp at all stages, especially at E12.5 (Fig. 2D). Therefore, we further analyzed global gene expression profile in E12.5 embryos even though they possibly included already-differentiating NCCs.

Expression profiles of cNCCs and tNCCs include genes related to carcinogenesis

To identity differences in the global mRNA profiles of Cp versus Tp, and EGFP$^+$ versus EGFP$^-$ cells, we performed transcriptome analyses using 3D-Gene (Toray Industries) of biologically duplicated samples from embryos at E12.5 when NCCs proliferate and start to differentiate. Representative scatter plots indicated differential molecular features of cNCCs and tNCCs (Fig. 3A). Compared with Tp, transcripts more enriched in Cp included molecules known as mesenchymal markers (*Cartl*, 31-fold; *Lhx8*, 29-fold; *Omd*, 23-fold; *Ibsp*, 14-fold; and *Akp2*, 12-fold) (Fig. 3B, left). This may reflect character of cNCCs giving rise to bone, cartilage, teeth, and connective tissues. NCC markers (*Pax7*, 21-fold; *Msx1*, 11-fold; *Barx1*, 10-fold; *Pax3*, 3.6-fold; and *PDGFRα* 2.8-fold) showed higher expression in cNCCs than in tNCCs (Fig. 3B, left). Unexpectedly, we identified several genes that have not previously been reported in association with NCCs but are suggested to be related with carcinogenesis. These genes showed higher expression in Cp than that in Tp (*Foxf1a*, 24-fold; *Rspo2*, 12-fold; *Penk1*, 10-fold; *S100a4*, 8-fold; and *Frk1*, 7-fold). Among these genes, we further confirmed the actual expression of the four genes (*Foxf1a*, *Rspo2*, *S100a4*, *Frk*) by qRT-PCR (Fig. 2C). These genes up-regulated in cNCC might provide a new insight for NC-originating tumorigenesis (see discussion).

Genes showing higher expression in Tp than that in Cp included a few well-known NCC markers, *Foxd3* (13-fold) and *Sox10* (6.7-fold) (Fig. 3B, right). In addition, several *Hox* genes showed remarkably higher expression in Tp, compared with that in Cp (*Hoxb6*, 313-fold; *Hoxb7*, 254-fold; *Hoxa5*, 87-fold; *Hoxb5*, 74-fold; *and Hoxd4*, 24-fold) (Fig. 3B, right); these *Hox* genes were also highly expressed in trunk EGFP$^-$ cells (Tn; Table S1).

We applied principal component analysis to summarize the transcriptome analyses for the four samples with biological duplication. On the biplot of the analysis, genes and samples are shown as points and vectors, respectively (Fig. 3C). The first and second principal components (PCs) clearly showed three distinctive sample groups, namely Cp, Tp, and the others (craniofacial EGFP$^-$ cells; Cn and Tn). Among the three sample groups, the Cp and Tp sample groups were particularly reproducible with biological duplicates, indicating that Cp and Tp sample groups clearly represented an NCC lineage.

To investigate the stem cell-like character of these samples, we selected 60 genes with known functions relating to stem cells (termed here as "stem cell genes") based on Gene Ontology (GO) annotations, and overlaid them on the biplot of the PC analysis (red points in Fig. 3C). Interestingly, most stem cell genes distributed along the Cp vector. We confirmed a large alteration in the expression of stem cell genes in Cp by applying an F-test to variances of the stem cell genes against all the genes on the microarray. The alteration of the stem cell genes was significantly larger than that of all genes in the Cp sample ($p = 0.0008$), while the alteration in the other three samples was not significant ($p = 1$). These results are considered to reflect the stem cell-like character in gene regulation of cNCCs.

We also performed clustering analyses of the four samples. Differentially expressed genes in Cp, Tp, Cn and Tn revealed considerable variation, which yielded seven probe clusters that showed a specific gene expression pattern for each sample (Fig. S1, Table S1). GO enrichment analyses of the clusters revealed that

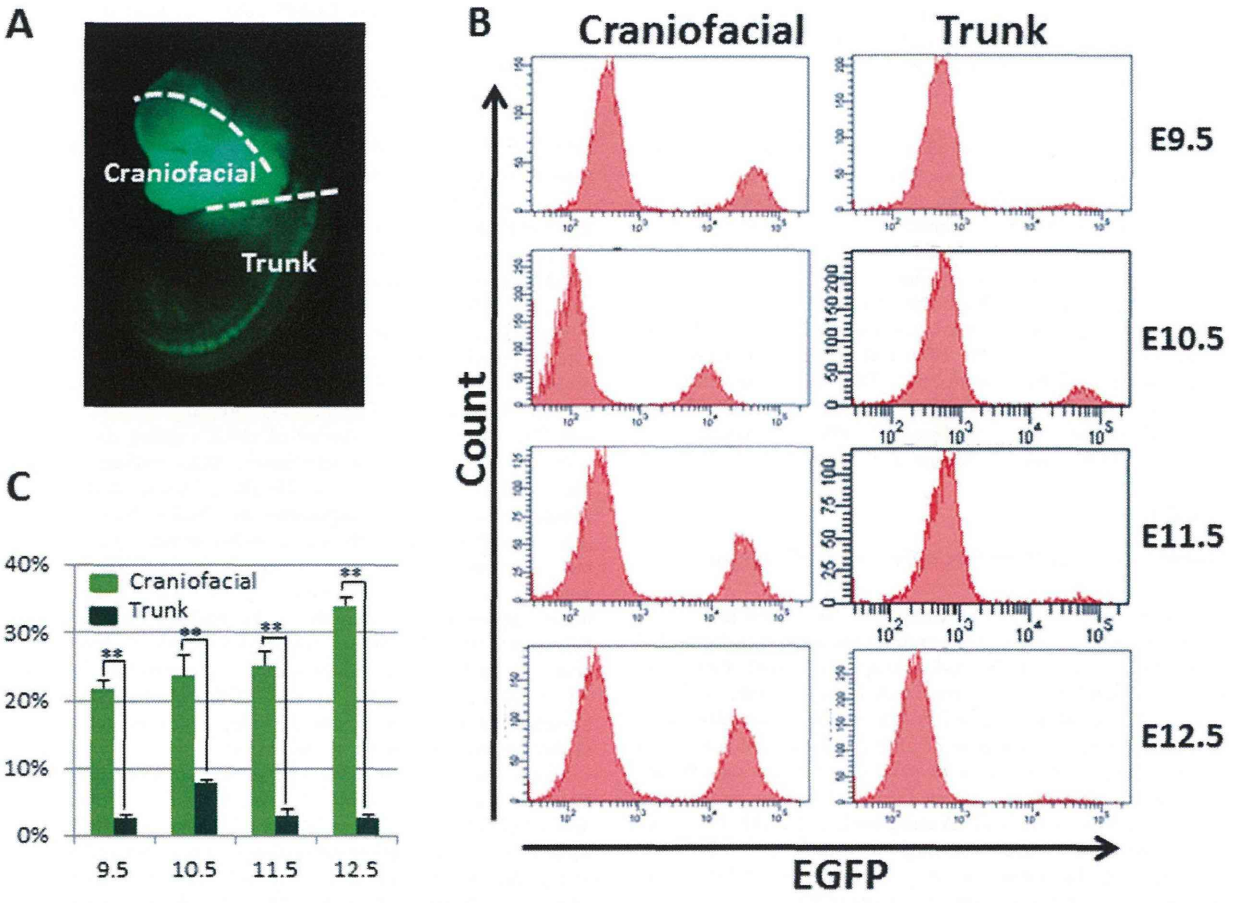

Figure 1. Isolation of NCCs from *P0-Cre/Floxed-EGFP* mouse embryos by fluorescence-activated cell sorting. (A) Craniofacial and trunk regions were indicated in the whole body by observation of direct EGFP fluorescence in E12.5 mice. (B) Representative EGFP-gated flow cytometric analysis charts clearly showed two populations, EGFP positive and negative at all examined embryonic ages. (C) The ratio of collected EGFP$^+$ cells showed a significantly higher frequency in the craniofacial region than that in the trunk region of all examined embryonic ages. Results were evaluated using the Student's *t*-test. (mean ± SD, n = 5 per group, **p<0.005).
doi:10.1371/journal.pone.0084072.g001

most of the genes specifically expressed in the four groups were in functional categories related to regulation of differentiation, development, and morphogenesis (see Tables S2, S3, S4, S5, S6, S7 for reference). Genes related to "Wnt signal" and "development" were highly enriched in Cp (Fig. S1A, Table S2). On the other hand, a category related to "nervous system development" was over-represented by up-regulated genes in Tp (Fig. S1C, Table S3). Genes related to "forebrain development" were up-regulated in Cn (Fig. S1D, Table S4). In addition, a category related to "anterior posterior pattern formation" was over-represented by up-regulated genes in both Tp and Tn (Fig. S1G, Table S7). These results indicate regional differences in the expression of developmental genes, particularly in EGFP$^+$ cells. In summary, cNCCs and tNCCs regions are extensively featured with their gene expression profiles that reflect their differential differentiation state and potential.

Differential gene expression profiles between NCCs and pluripotent stem cells

To estimate pluripotency of cNCCs and tNCCs, we examined the similarities of their gene expression to those of mouse iPSCs and ESCs cited from GEO database. Since both iPSC and ESC experiments (GEO accession: GSE18117 and GSE18813, respectively) used the same microarray platform with ours, we directly compared expression levels of genes on this platform. The scatter plot of the average of duplicate samples of Cp and Tp versus iPSCs or ESCs showed that both of the cNCCs and tNCCs similarly expressed lower levels of the well-known pluripotential markers (Fig. 4A–D). The expression levels of these markers were quite low in Cn and Tn (Data not shown). In contrast, the levels of NCC marker genes except for *FoxD3*, were lower in iPSCs and ESCs than in NCCs (Fig. 4A–D). In spite of significant alteration in expression of stem cell genes (Fig. 3C), the pluripotent marker genes showed similarly weak expression in Cp, Tp, Cn and Tn (Fig. 4A–D).

Confirmation of NCC-specificity in *P0-Cre/Floxed-EGFP* mouse embryo by immnohistchemistry

The expression patterns of the genes showing differential mRNA levels were further examined at the protein level by immunohistochemistry. For example, PDGFRα and PDGFRβ proteins were detected in craniofacial mesenchymal cells expressing EGFP, while Sox10 protein was selectively expressed in EGFP$^+$ cells located in the dorsal root ganglia (DRG), a major NC

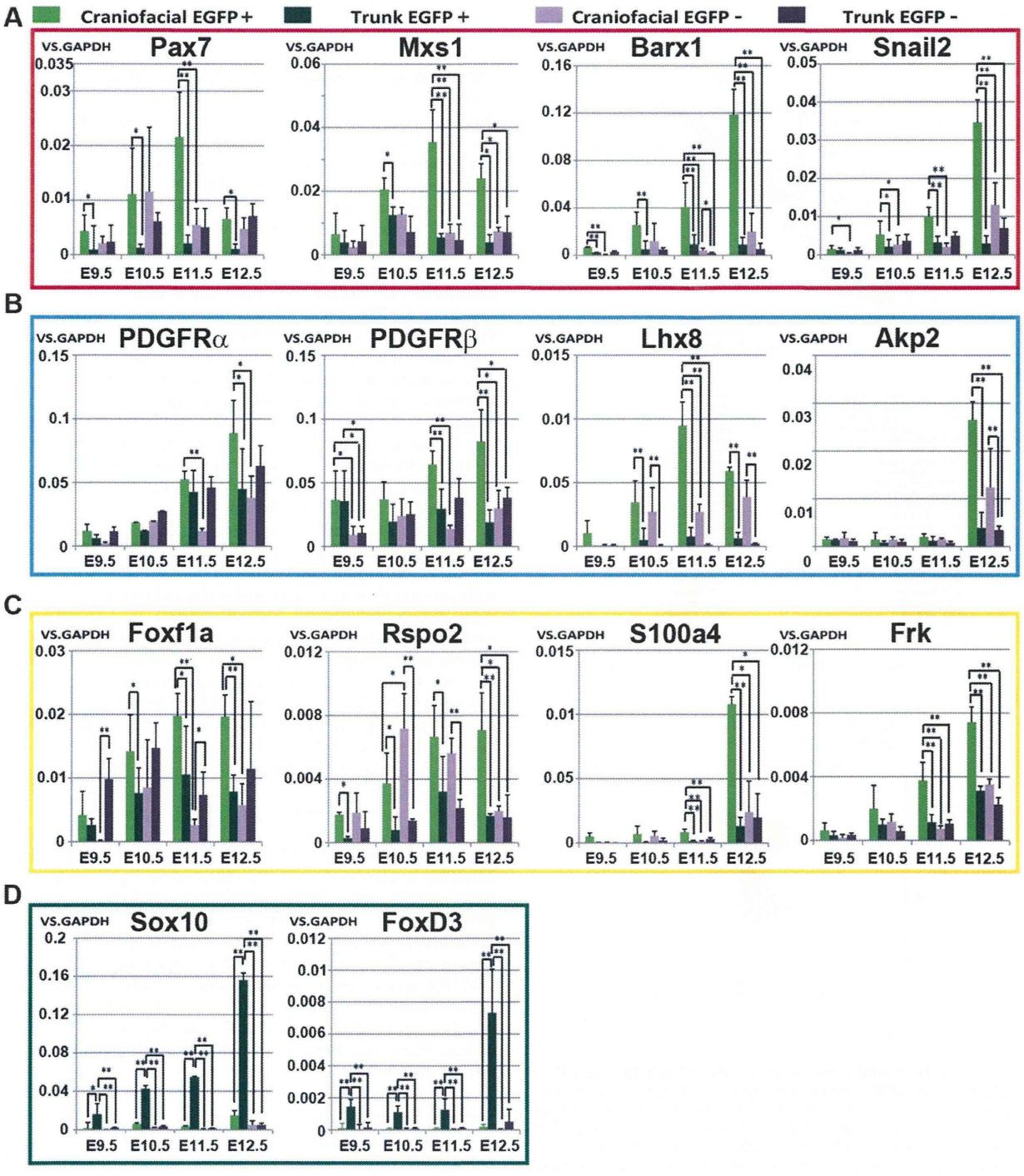

Figure 2. Quantitative PCR analysis of selected genes based on transcriptome analyses. EGFP^{+} and EGFP^{-} cells obtained from craniofacial and trunk regions at E9.5, E10.5, E11.5 and E12.5 were examined. (A) NCC markers up-regulated in cNCCs (Pax7, Msx1, Barx1 and snail2). (B) Mesenchymal markers up-regulated in cNCCs (PDGFRα, PDGFRβ, Lhx8 and Akp2. (C) Candidate markers up-regulated in cNCCs (Foxf1a, Rspo2, S100a4 and Frk). (D) NCC markers up-regulated in tNCCs (Sox10 and FoxD3). (mean±SD, n = 5 per group, *p<0.05, **p<0.005).
doi:10.1371/journal.pone.0084072.g002

derivative (Fig. S2). Considering the other staining results (Fig. S3), the majority of cNCCs showed the molecular character of mesenchymal derivatives, while the majority of tNCCs exhibited that of neural derivatives. These findings of the molecular features of NCCs are consistent with their differential states or fates as previously suggested (see Discussion). This again confirmed that

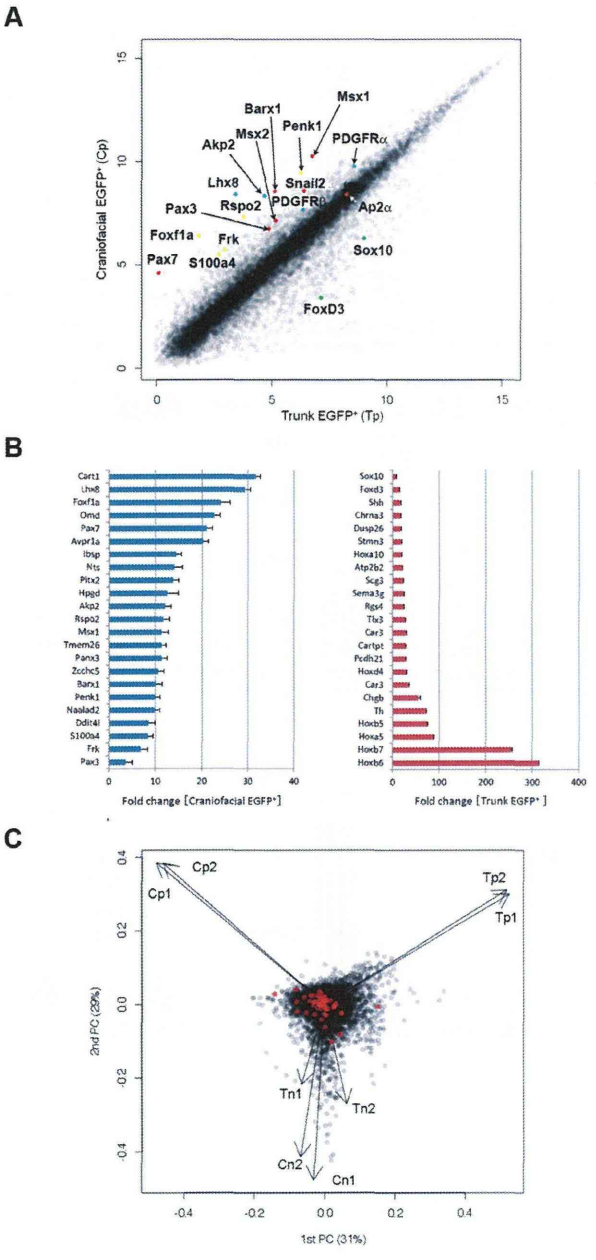

Figure 3. Differential expression profiles of cNCCs and tNCCs in *P0-Cre/Floxed-EGFP* mouse embryos. (A) Scatter plot of Craniofacial EGFP$^+$cells (Cp) and Trunk EGFP$^+$cells (Tp) as assessed by microarray analysis (3D-Gene; Toray Industries). (B) Most up-regulated genes in Craniofacial EGFP$^+$ cells (blue) and Trunk EGFP$^+$ cells (red), compared with those in the EGFP$^+$ cells of trunk and craniofacial regions, respectively. (C) Biplot of principal component analysis of the eight samples revealed three sample groups. Black dots indicate all genes and red dots indicate known stem cell genes selected from GO annotations. Cp, Tp, Cn; craniofacial EGFP$^-$ cells, and Tn; trunk EGFP$^-$ cells.
doi:10.1371/journal.pone.0084072.g003

EGFP$^+$ cells in *P0-Cre/floxed-EGFP* mouse reflect their origin as NC-derived.

Sphere-forming capability of cNCCs and tNCCs

We next assessed the stem cell-like characters of cNCCs and tNCCs by sphere-forming assays (Fig. 5). EGFP$^+$ and EGFP$^-$ cells dissociated from the craniofacial and trunk regions in E12.5 *P0-Cre/Floxed-EGFP* embryos were isolated by fluorescence-activated cell sorting, and cultured at 5×10^3 cells/ml in a serum-free sphere-forming medium containing growth factors, leukemia inhibitory factor (LIF) and B27 supplement as described previously [12]. Both EGFP$^+$ and EGFP$^-$ cell populations obtained from the two regions proliferated and formed spheres (Fig. 5B, C). This is quite contrast with the fact that few spheres are formed by adult EGFP$^-$ cells from the DRG, skin, whisker pad and bone marrow of *P0-Cre/Floxed-EGFP* mice [19]. We do not know whether this discrepancy is due to our different culture conditons (with LIF to enhance immature state or without) or to different stages of tissues (adult or embryonic). Among all four groups, the highest number of spheres was formed by craniofacial EGFP$^-$ cells (Fig. 5C). This may be because EGFP$^-$ cells contained neural stem cells located within the neural tube. Comparing regional difference of NCCs, a higher number of spheres were formed by craniofacial EGFP$^+$ cells than that by trunk EGFP$^+$ cells (Fig. 5C).

To assess the self-renewal capacity of these spheres, we conducted secondary sphere-forming assays. EGFP$^+$ and EGFP$^-$ spheres derived from both regions of *P0-Cre/Floxed-EGFP* mouse embryos were dissociated into single cells, and then cultured at the same density as that for primary spheres in sphere-forming medium. Secondary spheres were formed by all cells from primary spheres with a highest frequency in craniofacial EGFP$^-$ cells (Fig. 5D). Comparing regional difference, craniofacial EGFP$^+$ cells showed a higher level of secondary sphere formation than trunk EGFP$^+$ cells (Fig. 5D). This suggests that cNCCs have a higher capacity for self-renewal than that of tNCCs.

Next, we examined the molecular features of spheres cultured for 5 days *in vitro* (DIV). As expected, spheres formed by EGFP$^+$ cells highly expressed pluripotency markers Nanog, Oct3/4, PAR-4 and Sox2, with the exception of SSEA3 (Fig. 6). These spheres were also positive for NCC markers Ap2α, Ap2β, PDGFRα PDGFRβ and Sox10 (Fig. 6). The difference in expression levels of NCC markers in the spheres formed by craniofacial versus trunk EGFP$^+$ cells (Fig. 6) was in accordance with qRT-PCR and immunohistochemistry data of the embryos (Fig. 3 and S2). Expression of mesenchymal and NCC markers, *PDGFRα* and *PDGFRβ* was observed predominantly in spheres formed by craniofacial EGFP$^+$ cells, whereas *Sox10* expression was prominent in spheres formed by trunk EGFP$^+$ cells (Fig. 6). These results indicate that cultured spheres reproduce the differential features of cNCCs and tNCCs similarly to that *in vivo*.

Spheres derived from NCCs produce multiple cell types

To evaluate the differentiation potential of spheres, we cultured EGFP$^+$ and EGFP$^-$ spheres, obtained from the craniofacial and trunk regions of *P0-Cre/Floxed-EGFP* mouse embryos, in various differentiation media suitable for inducing individual tissue types (Fig. 7A). The four populations showed overlapping yet differential phenotypes in differentiating potentials.

Neuronal differentiation was induced by withdrawal of fibroblast growth factor 2 (FGF2), epidermal growth factor (EGF) and LIF from the medium. All four types of spheres frequently yielded neurons marked with βIII-tubulin (Fig. 7A), but a greater number of neurons were observed in spheres derived from the trunk EGFP$^+$ cells (Fig. 7B; 144 cells/field). The frequency of neurons in

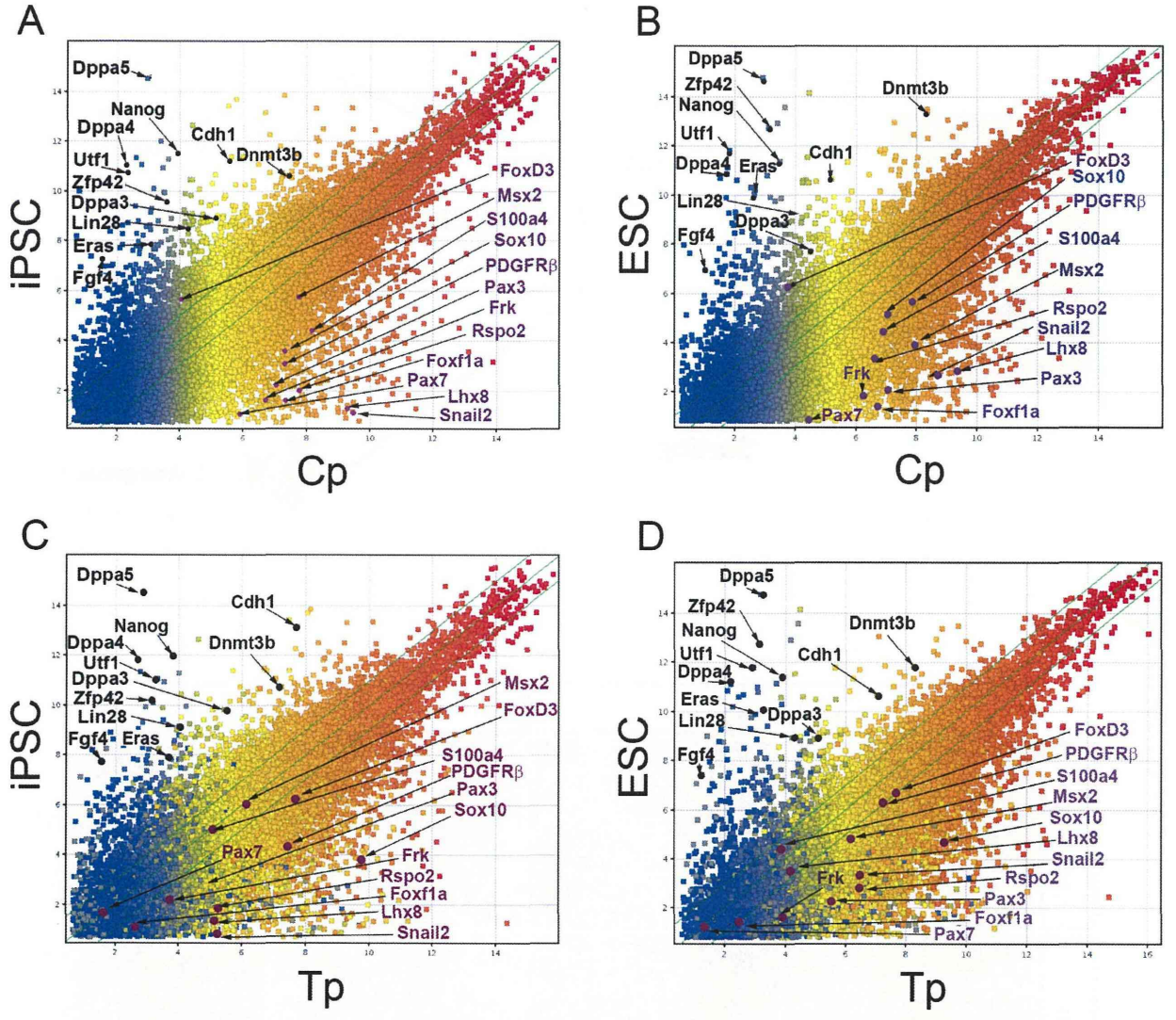

Figure 4. The comparison of gene expression analysis of Cp and/or Tp versus pluripotent stem cells. Schatter plot of Cp and iPSCs (A), Cp and ESCs (B), Tp and iPSCs (C), Tp and ESCs. Pluripotent markers were indicated by block charcters. NCC markers were indicated by violet characters.

doi:10.1371/journal.pone.0084072.g004

the other three types of spheres was almost identical (Fig. 7B; 69.7 cells/field for craniofacial EGFP$^+$; 58.0 cells/field for craniofacial EGFP$^-$; 58.5 cells/field for trunk EGFP$^-$). These results indicated that trunk EGFP$^+$ cells contained larger number of neuronal lineage NCCs than craniofacial EGFP$^+$ cells.

Glial differentiation was induced by addition of neuregulin (Fig. 7A, C, D). Only spheres derived from craniofacial and trunk EGFP$^-$ cells yielded O4-positive oligodendrocytes with a dramatically larger amount from the trunk EGFP$^-$ cells (Fig. 7C; four cells/field for craniofacial, and 30 cells/fields for trunk). S100β-positive glial cells including Schwann cells were obtained from all four types of spheres, with the greatest number in those derived from trunk EGFP$^+$ cells (Fig. 7D; 46.6 cells/fields for craniofacial EGFP$^+$; 111.7 cells/fields for trunk EGFP$^+$; 10.3 cells/fields for craniofacial EGFP$^-$; and 32 cells/fields for trunk EGFP$^-$). This quantification of neuronal and glial cell differentiation clearly showed that EGFP$^+$ spheres derived from the trunk region produced the highest frequency of neural lineages.

We further examined the potential to differentiate into mesenchymal lineages. EGFP$^+$ cells from craniofacial regions were capable of generating myofibroblastic (α-smooth muscle actin$^+$), adipogenic (oil red O$^+$), chondrogenic (alcian blue$^+$), and osteogenic (alizarin red$^+$) cells (Fig. 7A). Quantitative analyses were done in cases of myofibroblastic and adipogenic differentiation. EGFP$^+$ spheres derived from the craniofacial region showed the highest frequency of differentiation into myofibroblasts (Fig. 7E; 57 cells/fields for craniofacial EGFP$^+$; 30 cells/fields for trunk EGFP$^+$; 19.7 cells/fields for craniofacial EGFP$^-$; and 18 cells/fields for trunk EGFP$^-$), while trunk EGFP$^-$ cells exhibited the greatest number of adipocytes (Fig. 7F; 30.4 RFU for craniofacial EGFP$^+$; 21.0 RFU for trunk EGFP$^+$; 9.3RFU for craniofacial EGFP$^-$; and 117.2 RFU for trunk EGFP$^-$). This observation was expected because mesenchymal derivatives, such as adipocytes,

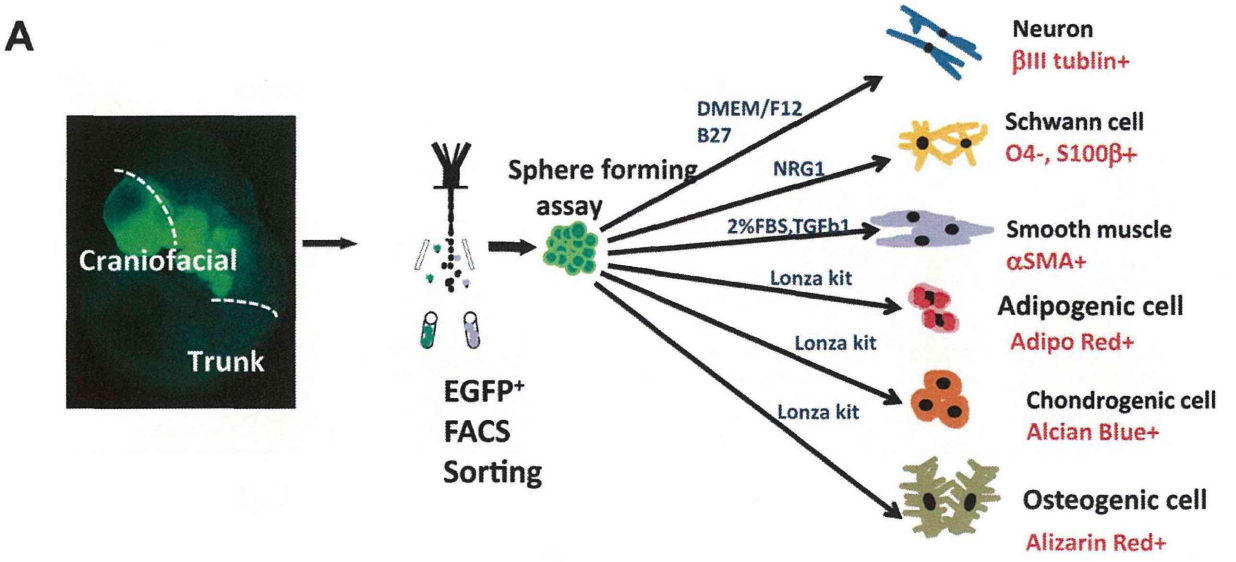
A
Craniofacial
Trunk
EGFP+
FACS
Sorting
Sphere forming
assay
DMEM/F12
B27
NRG1
2%FBS,TGFb1
Lonza kit
Lonza kit
Lonza kit
Neuron
βIII tublin+
Schwann cell
O4-, S100β+
Smooth muscle
αSMA+
Adipogenic cell
Adipo Red+
Chondrogenic cell
Alcian Blue+
Osteogenic cell
Alizarin Red+

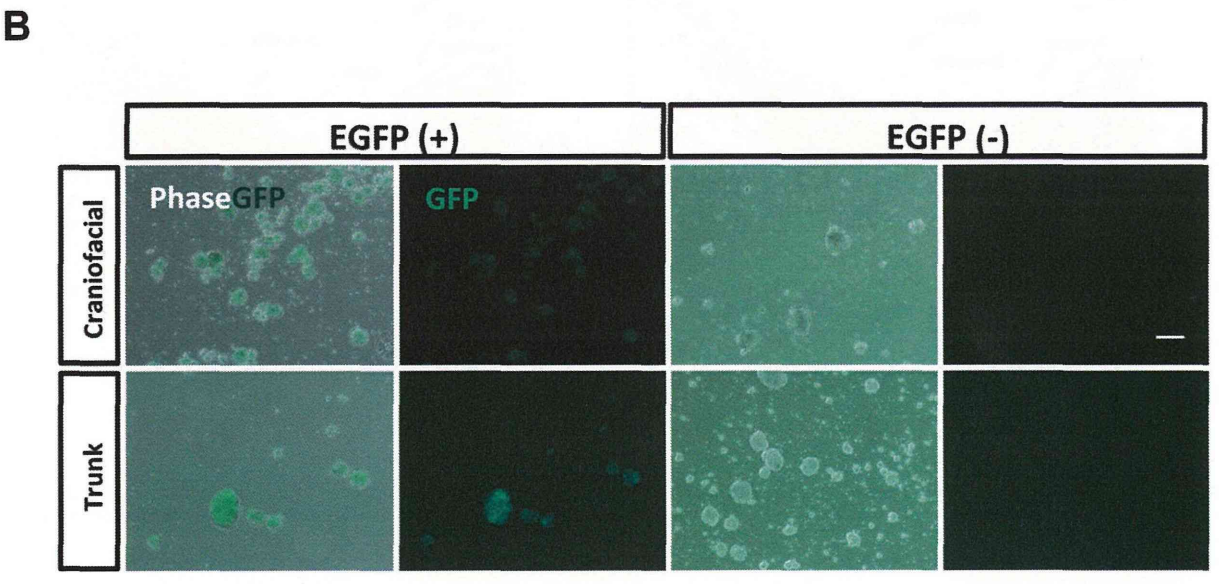
B
EGFP (+)
EGFP (-)
Craniofacial
Trunk
PhaseGFP
GFP

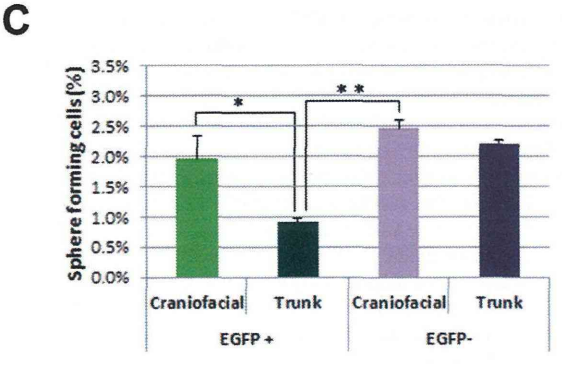
C
Sphere forming cells (%)
3.5%
3.0%
2.5%
2.0%
1.5%
1.0%
0.5%
0.0%
Craniofacial
Trunk
Craniofacial
Trunk
EGFP +
EGFP-

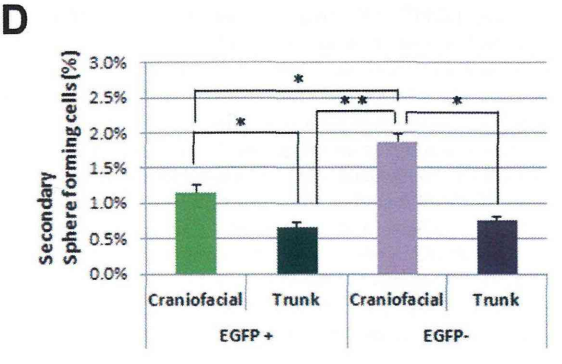
D
Secondary
Sphere forming cells (%)
3.0%
2.5%
2.0%
1.5%
1.0%
0.5%
0.0%
Craniofacial
Trunk
Craniofacial
Trunk
EGFP +
EGFP-

Figure 5. Sphere-forming capacity of EGFP$^+$ and EGFP$^-$ cells from craniofacial and trunk regions. (A) Schematic illustration of the experimental design for isolation and differentiation of P0-EGFP$^+$ cells from *P0-Cre/Floxed-EGFP* mouse embryos at E12.5. (B) Phase-contrast and direct EGFP fluorescence images showing spheres formed by EGFP$^+$ and EGFP$^-$ cells derived from craniofacial and trunk regions, respectively, after 5 DIV. Scale bar, 50 μm. (C, D) The percentage of sphere-forming cells assessed by culturing EGFP$^+$ and EGFP$^-$ cells from each region at a cell density of 5×10^3 cells/ml and counting the number of formed spheres. (mean ± SD; n = 5 per group, *p<0.05,**p<0.005). A significantly higher frequency of primary spheres (C) and secondary spheres (D) were formed by craniofacial EGFP$^+$ cells, compared with those formed by trunk EGFP$^+$ cells.
doi:10.1371/journal.pone.0084072.g005

can be differentiated from not only NCCs, but also the mesodermal cells that were observed among EGFP$^-$ cells, as speculated from a previous study showing mesodermal stem cells in P0-Cre/YFP mouse [20]. Qualitatively, chondrocytes differentiation was obvious in craniofacial EGFP$^+$ cells and trunk EGFP$^-$ cells, but not in other two populations (Fig. 7A). Osteocytes were differentiated from all three cell populations, except trunk EGFP$^+$ cells (Fig. 7A).

Taken altogether, NCCs purified as EGFP$^+$ cells from *P0-Cre/Floxed-EGFP* mouse embryos have a robust capacity for multipotent differentiation. It is of note that cNCCs have the broader

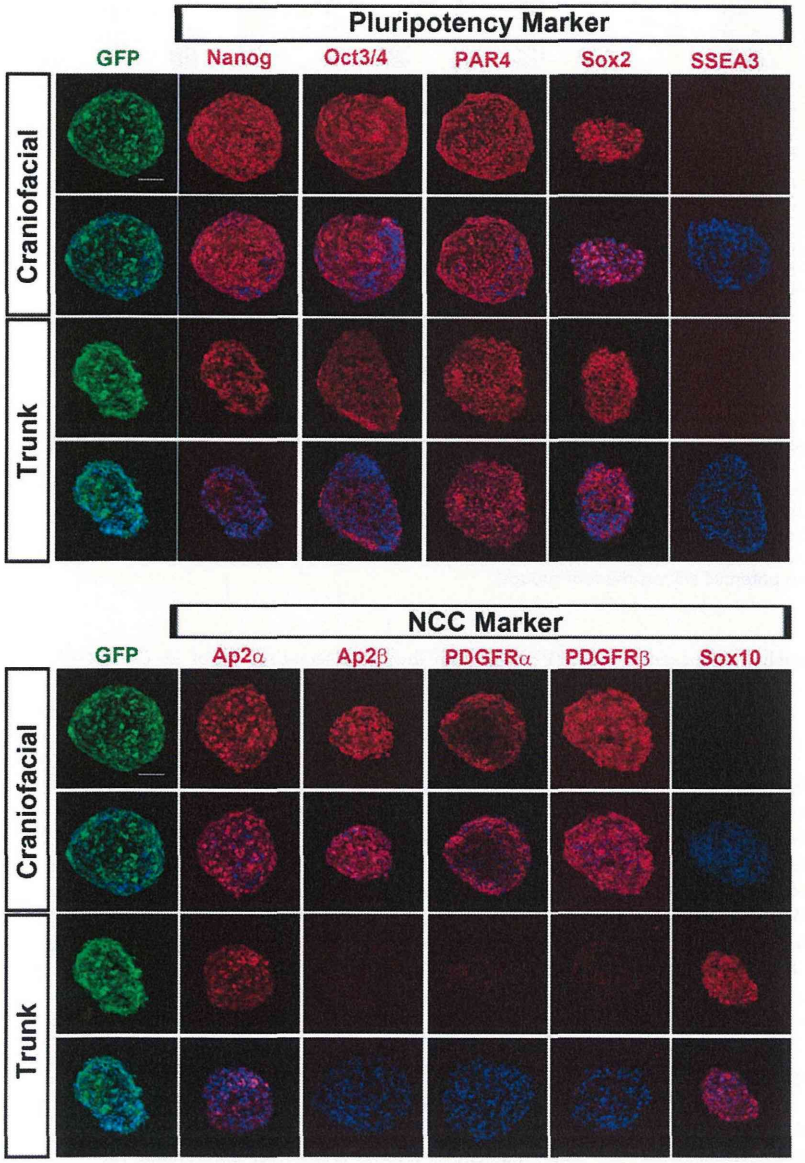

Figure 6. Immunocytochemical analyses of spheres derived from the EGFP$^+$ cells of craniofacial and trunk regions. (A) Expression of pluripotency markers (Nanog, Oct3/4, PAR4 and Sox2), except SSEA3, in EGFP$^+$ spheres derived from both regions. (B) Differential expression of NCC markers (Ap2α, Ap2β, PDGFRα, PDGFRβ and Sox10) in spheres between craniofacial and trunk EGFP$^+$ cells (scale bar; 20 μm).
doi:10.1371/journal.pone.0084072.g006

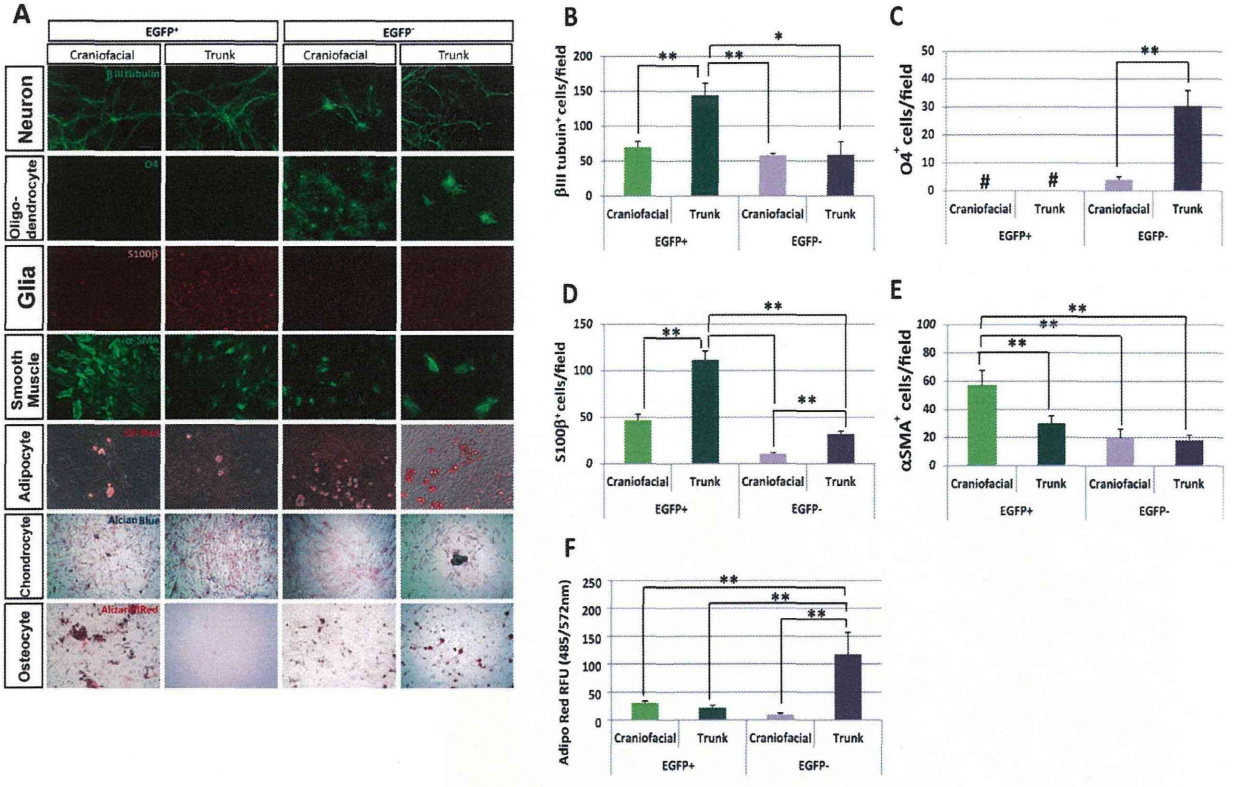

Figure 7. Differentiation potential of spheres derived from EGFP$^+$ and EGFP$^-$ cells from craniofacial and trunk regions. (A) Broad range of differentiation potential in spheres derived from craniofacial EGFP$^+$ cells. All groups of spheres differentiated into neurons, glial cells, myofibroblasts and adipocytes. Chondrocytes were differentiated from only spheres derived from craniofacial EGFP$^+$ cells and trunk EGFP$^-$ cells. Osteocytes were differentiated from all groups of spheres except for spheres derived from trunk EGFP$^+$ cells. (B–F) Spheres derived from trunk EGFP$^+$ cells showed peripheral neuronal lineages. Quantitative analyses of the potential for differentiation into neurons (B), oligodendrocytes (C), glial cells including Schwann cells (D), and myofibroblasts (E) by counting the number of cells positive for specific markers. (F) Quantification of adipocyte differentiation by relative fluorescence units (RFU). Excitation and emission of Adipo Red-stained cells was measured at 485 and 535 nm, respectively. Trunk EGFP$^-$ cells showed the highest differentiation potential among the four groups.
doi:10.1371/journal.pone.0084072.g007

differentiation potency for both neural and mesenchymal lineages than tNCCs.

Discussion

The expression and function of a limited number of NCC-specific molecules have been reported in previous studies [20–29]. Here, we identified differential features of cNCCs versus tNCCs at molecular and cellular levels in a systematic manner by combining flow cytometry, transcriptome analyses, sphere-forming assays, and differentiation assays, by the use of *P0-Cre/Floxed-EGFP* mouse embryos. Moreover, we identified a distinction in gene expression profiles of NCCs and pluripotent stem cells. Furthermore, we detected in NCCs up-regulation of genes that are related to carcinogenesis but have not previously been associated with NCCs. Our findings confirm specificity of P0-Cre-labeling of NC-derived cells and provide new insight on tumorigenesis originated from the NC.

Regarding regional difference in molecular and cellular characters of NCCs, we clearly identified genes enriched in cNCCs, namely *Pax7*, *Msx1*, *Barx1*, *Pax3*, *Msx2*, *snail2 and PDGFRα*. These molecules are known to be involved in the development of cNCCs [21,24–29]. This result in turn confirms that we could isolate NCCs or NC-derived immature cells as EGFP$^+$ cells from the craniofacial region of *P0-Cre/Floxed-EGFP* mouse embryos.

We also found several molecules that are known as mesenchymal (*Lhx8*), chondrogenic (*Cart1*), and osteogenic (*osteomodulin*, *Akp2*, and *Ibsp*) markers, with prominently higher expression in cNCCs than that in tNCCs. This result was reproduced in GO enrichment analysis. These molecular features are consistent with previous results obtained from transplantation experiments and clonal culture analyses that show the majority of cNCCs differentiate into mesenchymal derivatives [30–32].

In addition, Wnt signal-related genes are highly enriched in cNCCs as shown by GO enrichment analysis. Wnt signaling has been reported to play important roles in NC development. NC-delivered cranial structures and dorsal-root ganglion, but not sympathetic ganglion, were defective in *Wnt-1* and *Wnt-3b* null mice and *Wnt-1* and *Wnt-3b*-mediated *β-catenin* conditional knockout mice [33–35]. Especially craniofacial defects were strong in the later mice [33]. Thus, our findings further confirm that Wnt signaling is critical for the development of cNCCs.

The majority of tNCCs divergently differentiate into neuronal and glial derivatives [36]. This property is actually reflected in our GO enrichment analyses; *FoxD3* and *Sox10* showed relatively higher expression in tNCCs than that in cNCCs in microarray and also in qRT-PCR analyses. The expression of *FoxD3* is required

for NCC multipotency, selectively maintained in neural derivatives, and downregulated in mesenchymal derivatives [23]. *FoxD3* is also expressed considerably in pluripotent stem cells [37]. Mice carrying a mutation in *Sox10* demonstrate deformation in peripheral glia cells of NCC derivatives [38]. Expression of Sox10 continues in the glial lineages in the mouse embryo [39]. Thus, a high level of *Sox10* expression in tNCCs may reflect this situation. Taken together, our transcriptome analyses further confirmed distinct characters of tNCCs and cNCCs at molecular levels.

The stem cell-like character of NCCs has previously been studied *in vitro* using quail embryos [40]. Expression levels of pluripotent markers in cNCCs and tNCCs were weaker than those of iPSCs or ESCs. Similarly, NSCs taken from brain also show weaker expression of the pluripotent markers [41].

By sphere-forming assays, the tendency of primary sphere formation was relatively higher in cNCCs, craniofacial non-NCCs and trunk non-NCCs, and secondary sphere formation was the highest in the craniofacial non-NCCs. This tendency was also true for tertiary spheres. The higher frequency of sphere formation by craniofacial non-NCCs may be because they include neural progenitor cells from the forebrain. We observed robust expression of pluripotency markers and NCC markers in spheres derived from cNCCs and tNCCs. Interestingly, cNCCs showed a higher capacity for self-renewal than that of tNCCs. Significant alteration in the expression of stem cell genes in cNCCs also indicates the self-renewal potential of this tissue. Furthermore, as implicated by the differential molecular features, cNCCs and tNCCs showed a clear difference in terms of the cell types produced during differentiation assays. cNCCs differentiated into mesenchymal lineages such as osteocytes and chondrocytes, whereas tNCCs did not differentiate into either tissue. These results are in accordance with previous reports [42,43]. In our study, both cNCCs and tNCCs differentiated into adipocytes, as shown in a previous study [44], although trunk $EGFP^-$ cells produced the highest number of adipocytes. This result is quite reasonable, because trunk $EGFP^-$ cells include a relatively large proportion of mesodermal stem cells that can differentiate into osteocytes, chondrocytes and adipocytes. Regarding neural lineages, the highest number of neuronal cells and Schwann cells were differentiated from tNCCs. This is consistent with a previous report that the majority of tNCCs differentiate into neurons of the PNS, such as sympathetic, parasympathetic and sensory neurons, and Schwann cells [45]. Taken together, our comprehensive study clearly demonstrates that $EGFP^+$ cells isolated from *P0-Cre/floxed-EGFP* mouse at mid gestation show NCC features with accuracy and consistency and share a part of the stem cell-like character.

The stem cell-like character of NCCs prompts us to use NCCs that reside within adult tissues as a cell source for autologous transplantation in regenerative medicine. NCCs have been isolated from adult mouse heart [46], craniofacial tissues such as the mouse cornea [47] and iris [12], intestine [48] and from the human dental pulp [49], and evaluated for their properties as stem cells. Using *P0-Cre/Floxed-EGFP* mice would thus be beneficial for not only understanding craniofacial development and disorders, but also for potential resource of cells to induce multiple cell types needed for regenerative therapies.

The third aspect in our study is that we molecularly identified potential involvement of NCCs in tumorigenesis. As already mentioned above, activating Wnt signaling is one of the major mechanisms in formation of cancer [50]. We also identified up-regulation of cancer-related genes in NCCs. For example, *Frk*, a member of the small family of intracellular Src-related tyrosine kinases and a potential tumor suppressor [51], was originally identified in a human hepatoma cell line [52], and is expressed predominantly in epithelial tissues [49]. *S100a4*, a member of the S100 family of calcium-binding proteins, has been shown to activate pathways characteristic of cancer metastasis [53]. Given that NCCs share the stem cell-like potentials, expression of these cancer-related genes in NCCs may imply that NCCs can generally play important roles in carcinogenesis. Further analyses are required to examine potential up-regulation of these cancer-related genes in NCCs.

Involvement of NCCs in formation of tumors is intriguing. Melanoma is obviously derived from the NC-derived pigment cells in the skin [54]. Neuroblastoma and pheochromocytoma are formed in the adrenal gland and/or sympathetic ganglia, and thus believed to be NC-origin [55]. Our findings that NCCs show molecular features related with tumorigenesis might further suggest involvement of NCCs in other cancers. For example, origin of glioma is still enigmatic. A recent report has suggested oligodendrocyte precursor cells (OPCs) may participate in formation of glioma [56]. In this study, glioma has efficiently been induced by conditional genetic engineering using OPC-specific driver, NG2-Cre. We have recently reported in *P0-Cre/EGFP* mouse that NG2 is specifically expressed in cNCCs in the embryonic forebrain [17]. The majority of NCCs differentiated into the pericytes, but it seems that a small population of NCCs remains in an undifferentiated state [17]. The expression of NG2 in NCCs in the brain could thus provide insight that NG2-driven glioma formation might be derived also from NCCs. Furthermore, OPCs and pericytes express PDGFRα [57] and PDGFRβ [58], respectively, and it has been shown that PDGF is a strong inducer of glioma [59]. Our studies and previous reports have also shown expression of PDGF receptors in NCCs [17,20,60]. Therefore, it would be worth to try whether glioma can be induced by specifically targeting cNCCs. Future study on understanding NCCs might also contribute to prevent various tumors of NC-origin.

Supporting Information

Figure S1 Clustering on the data sets from general filtering of four populations. From these four populations (Cp, Tp, Cn, Tn), we identified 7 probe clusters. (A) Cp up-regulation (B) Cp down-regulation (C) Tp up-regulation (D) Cn up-regulation (E) Cp and Tp up-regulation (F) Cn and Tn up-regulation (G) Tp and Tn up-regulation.
(TIF)

Figure S2 Expression patterns of selected molecles based on transcriptome analysis. P0-Cre/Floxed-EGFP mouse embryos at E10.5 were immunostained (A–C). In the periocular mesenchyme as a representative craniofacial region, $EGFP^+$ cells were positive for PDGFRα and PDGFRβ but negative for Sox10 (D–F). In the dorsal root ganglion (DRG) as a representative trunk region, $EGFP^+$ cells were positive for Sox10, but negative for PDGFRα and PDGFRβ.
(TIF)

Figure S3 Immunohistochemistry of NCC markers. P0-Cre/Floxed-EGFP mouse embryos at E10.5 were immunostained (A, C, E). In the periocular mesenchyme as a representative craniofacial region, EGFP cells were positive for p75 but negative for NCAM and N-Cad (B, D, F). In the neural tissues as a representative trunk region, EGFP cells were positive for NCAM, N-Cad and p75.
(TIF)

Table S1 The 347 differentially expressed genes for clustering analyses. The following data are shown for each probe; probe ID, gene symbol of the corresponding gene, Log2 expression values in the eight samples including replicates, p value from ANOVA, Benjamini-Hochberg FDR, average expression values groups in the four tissue, expression range among the four tissue groups, and the cluster ID in Figure 3.
(XLSX)

Table S2 Top 10 enriched Gene Ontology Biological Process terms for cluster A.
(DOCX)

Table S3 Top 10 enriched Gene Ontology Biological Process terms for cluster C.
(DOCX)

Table S4 Top 10 enriched Gene Ontology Biological Process terms for cluster D.
(DOCX)

Table S5 Top 10 enriched Gene Ontology Biological Process terms for cluster E.
(DOCX)

Table S6 Top 10 enriched Gene Ontology Biological Process terms for cluster F.
(DOCX)

Table S7 Top 10 enriched Gene Ontology Biological Process terms for cluster G.
(DOCX)

Acknowledgments

We thank Drs. Narihito Nagoshi and Tadashi Nomura for critical reading of the manuscript, Ms. N. Konno for her expert technical assistance for cell sorting, and Ms. M. Kimura for technical support. We thank Drs. Kenichi Yamamura and Junichi Miyazaki for providing *P0-Cre* and *CAG-CAT-EGFP* TG mice, respectively. We are also grateful for the encouragement by all members of our laboratories. We thank Biomedical Research Core of Tohoku University Graduate School of Medicine for technical support.

Author Contributions

Conceived and designed the experiments: KH RH NO KN. Performed the experiments: KH NS EY. Analyzed the data: TO KH NO. Contributed reagents/materials/analysis tools: TO KH NO. Wrote the paper: KH NO. Financial supports: NO TN KN.

References

1. Le Douarin N, Kalcheim C. (1999) *The neural crest.* Vol. 36. Cambridge University Press.
2. Chung KF, Sicard F, Vukicevic V, Hermann A, Storch A, et al. (2009) Isolation of neural crest derived chromaffin progenitors from adult adrenal medulla. Stem Cells 27: 2602–2613.
3. Osumi-Yamashita N, Ninomiya Y, Doi H, Eto K (1994) The contribution of both forebrain and midbrain crest cells to the mesenchyme in the frontonasal mass of mouse embryos. Dev Biol 164:409–19.
4. White RM, Cech J, Ratanasirintrawoot S, Lin CY, Rahl PB, et al. (2011) DHODH modulates transcriptional elongation in the neural crest and melanoma. Nature 471: 518–22.
5. Xu L, Wang X, Wan J, Li T, Gong X, et al. (2012) Sonic Hedgehog pathway is essential for neuroblastoma cell proliferation and tumor growth. Mol Cell Biochem 364: 235–41.
6. von Levetzow C, Jiang X, Gwye Y, von Levetzow G, Hung L, et al. (2011) Modeling initiation of Ewing sarcoma in human neural crest cells. PLoS One 6: e19305.
7. Comino-Mendez I, Gracia-Aznárez FJ, Schiavi F, Landa I, Leandro-Garcia LJ, et al. (2011) Exome sequencing identifies MAX mutations as a cause of hereditary pheochromocytoma. Nat Genet 43: 663–7.
8. O'Neill ID (2011) Concise review: transmissible animal tumors as models of the cancer stem-cell process. Stem Cells 29: 09–14.
9. Yamauchi Y, Abe K, Mantani A, Hitoshi Y, Suzuki M, et al. (1999) A novel transgenic technique that allows specific marking of the neural crest cell lineage in mice. Dev Biol 212: 191–203.
10. Kawamoto S, Niwa H, Tashiro F, Sano S, Kondoh G, et al. (2000) A novel reporter mouse strain that expresses enhanced green fluorescent protein upon Cre-mediated recombination. FEBS letters 470: 263–268.
11. Kanakubo S, Nomura T, Yamamura KI, Miyazaki J, Tamai M, et al. (2006) Abnormal migration and distribution of neural crest cells in Pax6 heterozygous mutant eye, a model for human eye diseases. Genes Cells 11: 919–933.
12. Kikuchi M, Hayashi R, Kanakubo S, Ogasawara A, Yamato M, et al. (2011) Neural crest-derived multipotent cells in the adult mouse iris stroma. Genes Cells 16: 273–281.
13. Team R (2010) *R:* A language and environment for statistical computing. R Foundation for Statistical Computing Vienna Austria.
14. Maere S, Heymans K, M . Kuiper (2005) BiNGO: a Cytoscape plugin to assess overrepresentation of gene ontology categories in biological networks. Bioinformatics 21: 3448–3449.
15. Danielian PS, Muccino D, Rowitch DH, Michael SK, McMahon AP (1998) Modification of gene activity in mouse embryos in utero by a tamoxifen-inducible form of Cre recombinase. Curr Biol 8:1323–1326, S1–S2.
16. Gage PJ, Rhoades W, Prucka SK, Hjalt T (2005) Fate maps of neural crest and mesoderm in the mammalian eye. Invest Ophthalmol Vis Sci 46: 4200–4208.
17. Yamanishi E, Takahashi M, Saga Y, Osumi N (2012) Penetration and differentiation of cephalic neural crest-derived cells in the developing mouse telencephalon. Dev Growth Differ 54: 785–800.
18. Suzuki J, Yoshizakia K, Kobayashib T, Osumi N (2012) Neural Crest-derived Horizontal Basal Cells as Tissue Stem Cells in the Adult Olfactory Epithelium. Neurosci Res 75:112–120.
19. Nagoshi N, Shibata S, Kubota Y, Nakamura M, Nagai Y, et al. (2008) Ontogeny and multipotency of neural crest-derived stem cells in mouse bone marrow, dorsal root ganglia, and whisker pad. Cell Stem Cell 2:392–403.
20. Takashima Y, Era T, Nakao K, Kondo S, Kasuga M, et al. (2007) Neuroepithelial cells supply an initial transient wave of MSC differentiation. Cell 129: 1377–1388.
21. Conway SJ, Henderson DJ, Copp AJ (1997) Pax3 is required for cardiac neural crest migration in the mouse: evidence from the splotch (Sp2H) mutant. Development 124: 505–514.
22. Betters E, Liua Y, Kjaeldgaardb A, Sundströmc E, García-Castroa MI (2010) Analysis of early human neural crest development. Dev Biol 344: 578–592.
23. Mundell NA, Labosky PA (2011) Neural crest stem cell multipotency requires Foxd3 to maintain neural potential and repress mesenchymal fates. Development 138: 641–52.
24. Mansouri A, Stoykova A, Torres M, Gruss P (1996) Dysgenesis of cephalic neural crest derivatives in Pax7−/− mutant mice. Development 122: 831.
25. Satokata I, Maas R (1994) Msx1 deficient mice exhibit cleft palate and abnormalities of craniofacial and tooth development. Nat Genet 6: 348–356.
26. Tissier-Seta JP, Mucchiellia ML, Mark M, Mattei MG, Goridis C, et al. (1995) Barx1, a new mouse homeodomain transcription factor expressed in cranio-facial ectomesenchyme and the stomach. Mech Dev 51: 3–15.
27. Satokata I, Ma L, Ohshima H, Bei M, Woo I, et al. (2000) Msx2 deficiency in mice causes pleiotropic defects in bone growth and ectodermal organ formation. Nat Genet 24: 391–395.
28. Ros MA, Sefton M, Nieto MA (1997) Slug, a zinc finger gene previously implicated in the early patterning of the mesoderm and the neural crest, is also involved in chick limb development. Development 124: 1821–1829.
29. Soriano P (1997) The PDGF alpha receptor is required for neural crest cell development and for normal patterning of the somites. Development 124: 2691–700.
30. Platt JB (1894) Ectodermic origin of the cartilages of the head. Mass.
31. Stone LS (1926) Further experiments on the extirpation and transplantation of mesectoderm in Amblystoma punctatum. J Exp Zool 44: 95–131.
32. Stone L (1929) Experiments showing the role of migrating neural crest (mesectoderm) in the formation of head skeleton and loose connective tissue in Rana palustris. Dev Genes Evol 118: 40–77.
33. Brault V, Moore R, Kutsch S, Ishibashi M, Rowitch DH, et al. (2001) Inactivation of the (β)-catenin gene by Wnt1-Cre-mediated deletion results in dramatic brain malformation and failure of craniofacial development. Development 128: 1253–1264.
34. Ikeya M, Lee SMK, Johnson JE, McMahon AP, S . Takada (1997) Wnt signalling required for expansion of neural crest and CNS progenitors. Nature 389: 966–970.
35. Wu J, Saint-Jeannet JP, Klein PS (2003) Wnt-frizzled signaling in neural crest formation. Trends Neurosci 26: 40–45.
36. Teillet MA, Kalcheim C, Le Douarin NM (1987) Formation of the dorsal root ganglia in the avian embryo: segmental origin and migratory behavior of neural crest progenitor cells. Dev Biol 120: 329–47.
37. Hanna LA, Foreman RK, Tarasenko IA, Kessler DS, Labosky PA (2002) Requirement for Foxd3 in maintaining pluripotent cells of the early mouse embryo. Genes Dev 16: 2650–2661.

38. Britsch S, Goerich DE, Riethmacher D, Peirano RI, Rossner M, et al. (2001) The transcription factor Sox10 is a key regulator of peripheral glial development. Genes Dev 15: 66–78.
39. Kuhlbrodt K, Herbarth B, Sock E, Hermans-Borgmeyer I, Wegner M (1998) Sox10, a novel transcriptional modulator in glial cells. J Neurosci 18: 237–250.
40. Trentin A, Glavieux-Pardanaud C, Le Douarin NM, Dupin E (2004) Self-renewal capacity is a widespread property of various types of neural crest precursor cells. (2004) Proc Natl Acad Sci U S A 101: 4495.
41. Kim JB, Zaehres H, Wu G, Gentile L, Ko K, et al. (2008) Pluripotent stem cells induced from adult neural stem cells by reprogramming with two factors. Nature 454: 646–650.
42. Noden DM (1983) The role of the neural crest in patterning of avian cranial skeletal, connective, and muscle tissues. Dev Biol 96: 144–165.
43. Stemple DL, Anderson DJ (1992) Isolation of a stem cell for neurons and glia from the mammalian neural crest. Cell 71: 973–985.
44. Billon N, Iannarelli P, Monteiro MC, Glavieux-Pardanaud C, Richardson WD, et al. (2007) The generation of adipocytes by the neural crest. Development 134: 2283–92.
45. Christiansen JH, Coles EG, Wilkinson DG (2000) Molecular control of neural crest formation, migration and differentiation. Curr Opin Cell Biol 12:719–724.
46. Tomita Y, Matsumura K, Wakamatsu Y, Matsuzaki Y, Shibuya I, et al. (2005) Cardiac neural crest cells contribute to the dormant multipotent stem cell in the mammalian heart. J Cell Biol 170: 1135–1146.
47. Yoshida S, Shimmura S, Nagoshi N, Fukuda K, Matsuzaki Y, et al. (2006) Isolation of multipotent neural crest-derived stem cells from the adult mouse cornea. Stem Cells 24: 2714–22.
48. Young HM, Bergner AJ, Müller T (2002) Acquisition of neuronal and glial markers by neural crest–derived cells in the mouse intestine. J Comp Neurol 456: 1–11.
49. Laino G, D'Aquino R, Graziano A, Lanza V, Carinci F, et al. (2005).A new population of human adult dental pulp stem cells: a useful source of living autologous fibrous bone tissue (LAB). J Bone Miner Res 20: 1394–1402.
50. Wend P, Holland JD, Ziebold U, Birchmeier W (2010) Wnt signaling in stem and cancer stem cells. Semin Cell Dev Biol 21: 855–863.
51. Chandrasekharan S, Qju TH, Alkharouf N, Brantley K, Mitchell JB, et al. (2002) Characterization of mice deficient in the Src family nonreceptor tyrosine kinase Frk/rak. Mol Cell Biol 22: 5235–5247.
52. Lee J, Wangb Z, Luoha SM, Wooda WI, Scadden DT (1994) Cloning of FRK, a novel human intracellular SRC-like tyrosine kinaseencoding gene. Gene 138: 247–251.
53. Mishra SK, Siddique HR, Saleem M (2011) S100A4 calcium-binding protein is key player in tumor progression and metastasis: preclinical and clinical evidence. Cancer Metastasis Rev 31: 163–172.
54. White RM, Cech J, Ratanasirintrawoot S, Lin CY, Rahl PB, et al. (2011) DHODH modulates transcriptional elongation in the neural crest and melanoma. Nature 471: 518–522.
55. Schulte JH, Lindner S, Bohrer A, Maurer J, De Preter K, et al. (2012) MYCN and ALKF1174L are sufficient to drive neuroblastoma development from neural crest progenitor cells. Oncogene 32: 1059–1065
56. Liu C, Sage JC, Miller MR, Verhaak RGW, Hippenmeyer S, et al. (2011) Mosaic analysis with double markers reveals tumor cell of origin in glioma. Cell 146: 209–21.
57. Kang SH, Fukaya M, Yang JK, Rothstein JD, Bergles DE (2010) $NG2^+$ CNS glial progenitors remain committed to the oligodendrocyte lineage in postnatal life and following neurodegeneration. Neuron 68: 668–681.
58. Hellstrom M, Kalen M, Lindahl P, Abramsson A, Betsholtz C (1999) Role of PDGF-B and PDGFR-beta in recruitment of vascular smooth muscle cells and pericytes during embryonic blood vessel formation in the mouse. Development 126: 3047–3055.
59. Calzolari F, Malatesta P (2009) Recent insights into PDGF-induced gliomagenesis. Brain Pathol 20: 527–538.
60. Morikawa S, Mabuchi Y, Niibe K, Suzuki S, Nagoshi N, et al. (2009) Development of mesenchymal stem cells partially originate from the neural crest. Biochem Biophys Res Commun 379: 1114–1119.

Current Eye Research, 2013; 38(11): 1133–1141

ISSN: 0271-3683 print / 1460-2202 online
DOI: 10.3109/02713683.2013.807932

informa
healthcare

ORIGINAL ARTICLE

Simulated Visual Fields Produced from Macular RNFLT Data in Patients with Glaucoma

Mai Takahashi[1]*, Kazuko Omodaka[1]*, Kazuichi Maruyama[1], Takuhiro Yamaguchi[2], Noriko Himori[1], Yukihiro Shiga[1], Morin Ryu[1], Hiroshi Kunikata[1] and Toru Nakazawa[1]

[1]*Department of Ophthalmology and* [2]*Department of Biostatics, Tohoku University Graduate School of Medicine, Sendai, Miyagi, Japan*

ABSTRACT

Purpose: We investigated in detail the correlation between structure and function in the macula, and whether optical coherence tomography (OCT)-measured macular structure could be used to simulate the visual field.

Materials and methods: This study comprised 60 eyes of 34 patients with open angle glaucoma (Anderson-Patella classification). To assess macular function, reliable data from the Humphrey field analyzer (HFA, SITA-standard, 10-2 program) for threshold, total deviation (TD), and pattern deviation (PD) were used. To assess macular structure, thickness data for the retinal nerve fiber layer (RNFL), ganglion cell complex (GCC), and ganglion cell layer plus inner plexiform layer (GCL + IPL) from macular OCT maps (3D OCT-2000, Topcon) were analyzed. Spearman's coefficient of correlation analysis was performed to determine the significance of the correlation, as well as the formula for simulation. The formula was used to calculate the simulated threshold, TD, and PD values. The simulation method was validated by comparing results for simulated and actual visual fields in a new data set of 29 eyes from glaucoma patients.

Results: In most test points, macular function and the layer-by-layer structure were significantly correlated, however, the distribution of highly-correlated points varied. Simulated grayscale maps of the visual field based on the formula of regression line for RNFLT and thresholds were similar to actual visual fields. There was a significant correlation between simulated visual fields created from RNFLT, GCC and GCL + IPL data and actual average threshold values in all 68 test points ($r = 0.63$–0.87, $p < 0.001$) and TD ($r = 0.62$–0.86, $p < 0.001$).

Conclusion: We found that there was a significant correlation between structure and function in the macular area, and that simulated visual fields from RNFLT data reflected actual visual fields. Such a simulation of macular function from OCT parameters may be useful in assessing glaucoma in patients who have difficulty undergoing actual visual field examinations.

Keywords: Central visual field, myopia, simulation, visual acuity

INTRODUCTION

Glaucoma is a complex, heterogeneous, and multifactorial disease. It is the second most common cause of blindness, affecting approximately 70 million people worldwide.[1] The prevalence of glaucoma increases with age,[2] and as the country's population ages, the increasing frequency of visual impairment caused by this disease is becoming a serious issue.

Glaucoma is characterized by glaucomatous optic neuropathy, corresponding to a progressive degeneration of retinal ganglion cells (RGCs) and their axons, which comprise the retinal nerve fiber layer (RNFL).[3] At present, no definitive examination technique for the quantification of RGC loss has been established. Therefore, cupping progression, RNFL thinning, and visual field tests are the main methods used to monitor the longitudinal progress of glaucoma.

Received 23 January 2013; revised 22 April 2013; accepted 16 May 2013; published online 9 July 2013

*These authors contributed equally to this work.

Correspondence: T. Nakazawa, Department of Ophthalmology, Tohoku University Graduate School of Medicine, 1-1 Seiryo-machi, Aoba-ku, Sendai, Miyagi 980-8574, Japan. Tel: +81-22-717-7294. Fax: +81-22-717-7298. E-mail: ntoru@oph.med.tohoku.ac.jp

Since its introduction by Huang et al.,[4] optical coherence tomography (OCT) has been used to measure circumpapillary retinal nerve fiber layer thickness (cpRNFLT), a useful parameter for glaucoma detection and follow-up. OCT evaluation has become a requirement in objective examinations of glaucoma. Despite many reports that glaucoma patients also exhibit reduced macular thickness,[5–8] however, testing of the macular area has not become a supplement to OCT measurement of cpRNFLT, because the accuracy of the former as a diagnostic parameter has failed to be established.[5–8] Recently, however, segmentation algorithms for spectral domain (SD) technology have improved significantly, and several research groups have been able to visualize each retinal layer in the macular area, including the ganglion cell complex (GCC), which comprises the layer from the RNFL to the inner plexiform layer (IPL), and the ganglion cell layer plus IPL (GCL + IPL).[9] Recent studies[10,11] have shown that measurement of macular GCC thickness holds the same value for glaucoma diagnosis as measurement of cpRNFLT.

A recent study by our team has demonstrated that temporal cpRNFLT, including the papillomacular bundle, is significantly correlated to visual acuity (LogMAR units, correlated coefficient: −0.4) in patients with glaucoma. The cut off value for decreased decimal visual acuity less than 0.9 was 38 μm.[12] The pathogenesis of this decreased visual acuity may be related to myopia and decreased tissue blood flow in the temporal optic disc.[12] These data suggest that temporal cpRNFLT may be a useful biomarker for assessing glaucomatous nerve fiber defects.

In this study, we first investigated the correlation between the thickness of specific retinal layers of the macular OCT map (RNFL, GCC and GCL + IPL) and Humphrey field analyzer (HFA) parameters including threshold, total deviation (TD) and pattern deviation (PD) of the central visual field (HFA 10-2). Next, we calculated the formula for linear regression analysis for a series of test points on the retina; each point contained corresponding data for RNFLT from a macular OCT map, and threshold values from 10-2 HFA tests. Finally, we investigated the possibility of using these data to create a simulated visual field. These data may help with the management of glaucoma in patients.

MATERIAL AND METHODS

Inclusion Criteria

This retrospective, cross-sectional study comprised a total of 60 eyes of 34 Japanese adult patients with OAG (10 with POAG, 24 with NTG). All the patients exhibited glaucomatous optic neuropathy. Glaucoma patients with visual field loss close to visual fixation, decreased visual acuity and glaucomatous damage to the papillomacular bundle were introduced to the outpatient unit for neuroprotective treatment at Tohoku University Hospital. Subsequent routine testing included HFA 10-2. The inclusion criteria were: (1) diagnosis of OAG, including POAG and NTG, (2) a spherical equivalent refractive error of >−8.00 diopters and (3) a glaucomatous visual field meeting the Anderson-Pattela classification.[13] The exclusion criteria were: (1) decimal visual acuity <0.3 and (2) presence of macular disease, such as macular edema, macular degeneration or premacular fibrosis. A total of 29 eyes of 29 Japanese adult patients with OAG were recruited to validate the simulation system.

The baseline clinical parameters recorded for each patient were age, gender and refractive error. The baseline best-corrected visual acuity was measured with a standard Japanese decimal visual acuity chart, and converted to the logarithm of the minimum angle of resolution (logMAR) for statistical analysis. Intra ocular pressure (IOP) was measured by Goldmann applanation tonometry at the time of the initial diagnosis of OAG, before the use of any glaucoma medications.

The study adhered to the tenets of the Declaration of Helsinki, and the protocols were approved by the Clinical Research Ethics Committee of Tohoku University Graduate School of Medicine.

Visual Field Analysis

Threshold, TD and PD values at each test points and mean deviation (MD) and pattern standard deviation (PSD) were measured using the Swedish interactive threshold algorithm (SITA)-standard strategy of the HFA 30-2 or 10-2 programs (Carl Zeiss Meditec, Dublin, CA). HFA examinations were performed within three months of the OCT measurements. Threshold, TD, and PD values were taken only from reliably measured visual fields (<20% fixation errors, <33% false-positive results and <33% false-negative results). Since some glaucoma patients in this study had decreased visual acuity, due to glaucomatous damage to the papillomacular bundle, we chose to loosen our definition of reliability for HFA results.

OCT Macular Map

Macular RNFL, GCC and GCL + IPL thickness were obtained with 3D OCT-2000 and measured with the equipped software (version 8.00; Topcon, Inc.). First, a macular cube scan of a 7 × 7 mm square area was obtained, from which a 6 × 6 mm area was selected for analysis. This smaller area was centered on the fovea

and corresponded to the central 20° of the macula. Next, a 10×10 grid, with points separated by two degrees, was overlaid on the scan, and the embedded 3D OCT program automatically calculated the thickness of the retinal layers at each of these points. Thus, 68 points from the resulting macular OCT map corresponded to the 68 test points of the HFA 10-2 program. These tested points were used for analysis. Images were excluded if the image quality was less than 60.

Correlation Between OCT and HFA

When the analysis included both the right and the left eyes, the left eye was flipped across the vertical midline to give the appearance of a right eye, and all structural data was flipped across the horizontal midline for display in "field view". We superimposed 68 test points from the HFA 10-2 analysis with a corresponding 10×10 grid ($6 \times 6\,mm^2$) from the OCT significance map. In order to avoid the magnification effect with elongation of the axial length, 3D OCT-2000 has an automated function to adjust the length of the scan lines to the patient's refraction. Calibration of the HFA, with a schematic eye, was also performed. For each test point, we determined the correlation for threshold, TD and PD from the HFA parameters, and RNFL, GCC, GCL + IPL from the OCT parameters.

Simulation of Visual Fields from OCT Macular Map

We blotted the measured OCT macular parameters (for the RNFL, GCC and GCL + IPL) and the measured HFA 10-2 parameters (threshold, TD and PD). We next solved the formula of linear regression analysis for each test point, and then used the formula to calculate a simulation of visual field sensitivity. We constructed a simulated grayscale visual field using 10 shades of gray, representing 5 dB steps. Finally, we determined the correlation of the mean value of the calculated visual field obtained with OCT, and the mean of the measured visual field values for the new data set, in 29 eyes from glaucoma patients (10 with POAG, 19 with NTG).

Statistical Analysis

Spearman's correlation analysis was used to determine the correlation between the structural examination (RNFLT, GCC, and GCL + IPL from 3D OCT-2000) and the results of a functional examination (threshold, TD and PD from the HFA 10-2). It was also used to determine the correlation between the measured and simulated visual field values in both the original group and in different data sets. The significance level was set at $p < 0.05$. The statistical analysis was performed with JMP software (Pro version 9.0.2, SAS Institute Japan Inc., Tokyo, Japan).

RESULTS

To simulate a visual field using data for the structure of the macula, we investigated in detail the correlation between the visual field and macular retinal layer thickness in a series of test points. We aligned the blocks of an OCT macular map to test points from the HFA 10-2 so that they had a positional correspondence (Figure 1). The demographic data used in this study is listed in Table 1. The average age was 65.7 ± 11.1 years, average spherical equivalent was -2.8 ± 2.2 diopters, average logMAR visual acuity was 0.08 ± 0.28, average HFA 30-2 MD was -12.1 ± 8.9 dB, average baseline IOP was 19.7 ± 7.1 mmHg and average cpRNFLT was 79.3 ± 14.8 μm.

The correlation of the OCT macular map to each parameter used in this study is listed in Table 2. Macular parameters for the thickness of all retinal layers were significantly correlated to HFA 30-2 MD (RNFLT: $r = 0.49$, GCC: $r = 0.44$, GCL + IPL: $r = 0.33$). HFA 30-2 PSD was significantly correlated to RNFLT ($r = -0.49$) and GCC ($r = -0.37$) but not to GCL + IPL ($r = -0.22$). HFA 10-2 MD was significantly correlated to RNFLT ($r = 0.76$), GCC ($r = 0.72$), and GCL + IPL ($r = 0.55$). HFA 10-2 PSD was not correlated to RNFLT ($r = -0.17$), GCC ($r = 0.06$), or GCL + IPL ($r = 0.18$). LogMAR was significantly correlated to the thickness of both macular layers (RNFLT: $r = -0.35$, GCC: $r = -0.41$), as well as GCL + IPL ($r = -0.39$). CpRNFLT was correlated to RNFLT ($r = 0.34$), GCC ($r = 0.33$) and GCL + IPL ($r = 0.31$). None of these macular layer thicknesses were significantly correlated to the spherical equivalent or baseline IOP ($r = -0.02$ and 0.12, respectively).

To find the correlation between RNFLT and each HFA parameter, we performed a single regression analysis (Figure 1E), blotted according to the power of correlation coefficient shown in Figure 2(A)–(C), and calculated the formula for each test point. There was a significant correlation between RNFLT and the threshold (correlation coefficient ranging; $r = 0.43$–0.87) and TD ($r = 0.52$–0.87) in all 68 test points (Figure 2A and B). Generally, the correlation coefficient was lowest in the nasal area. There was a significant correlation between RNFLT and PD ($r = 0.35$–0.69) in all but six test points (Figure 2C). The correlation coefficient with PD was lower than that with threshold or TD.

GCC was significantly correlated with the threshold ($r = 0.40$–0.85) and TD ($r = 0.41$–0.86) in all 68 test points (Figure 2D and E). The correlation coefficient

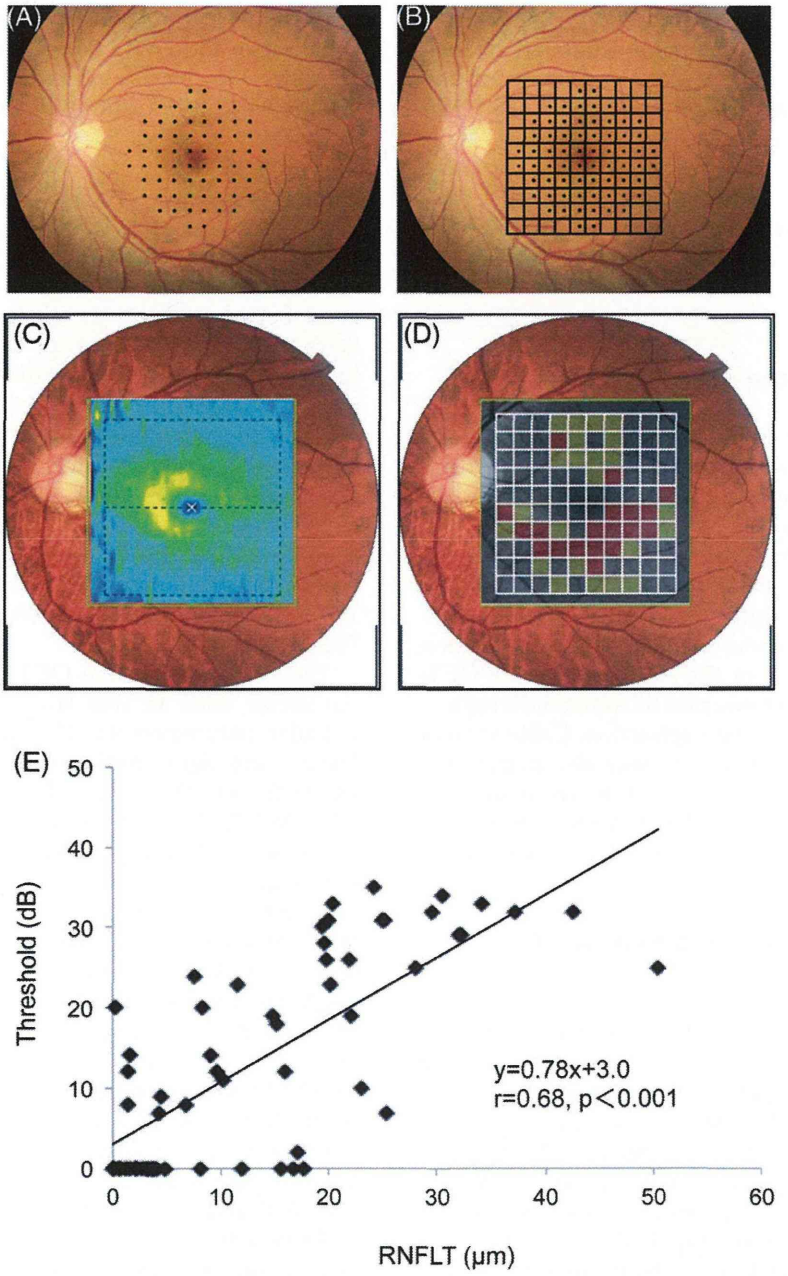

FIGURE 1 Correspondence for 68 HFA 10-2 test points from and 10 × 10 3D OCT-2000 grids. (A) All 68 HFA 10-2 test points. (B) One to one correspondence between each HFA 10-2 test point and a 10 × 10 3D OCT-2000 grid from. (C) 3D OCT-2000 map of the RNFL, GCC and GCL + IPL in the macula. (D) Significance map of macular thickness. (E) Blot graph showing the correlation between measured OCT thickness and threshold values, with the formula of linear regression analysis for each test point.

TABLE 1 Demographic data for the glaucoma patients in this study.

Sex Male: Female	43(72%) : 17(28%)
Age (yrs)	65.7 ± 11.1
Spherical equivalent (D)	−2.8 ± 2.2
Visual acuity (logMAR)	0.08 ± 0.28
MD of HFA30-2(dB)	−12.1 ± 8.9
Pretreated IOP (mmHg)	19.7 ± 7.1
cpRNFLT(μm)	79.3 ± 14.8

was lowest in the upper nasal area. There was a significant correlation between GCC and PD ($r = 0.28$–0.65) in all but seven test points (Figure 2F). The correlation coefficient with PD was lower than that with threshold or TD.

The thickness of the GCL + IPL was significantly correlated with the threshold ($r = 0.26$–0.81), TD ($r = 0.27$–0.81) and PD ($r = 0.24$–0.59) in the central circular area (Figure 2G–I). Peripheral test points, however, showed no significant correlation between

TABLE 2 The relationship between the thickness of each macular retinal layer and clinically-measured parameters.

	RNFL		GCC		GCL+IPL	
	r	*p*	*r*	*p*	*r*	*p*
MD(HFA30-2)	**0.49**	**<0.001**	**0.44**	**<0.001**	**0.33**	**0.013**
PSD(HFA30-2)	**−0.49**	**<0.001**	**−0.37**	**0.005**	−0.22	0.09
MD(HFA10-2)	**0.76**	**<0.001**	**0.72**	**<0.001**	**0.55**	**<0.001**
PSD(HFA10-2)	−0.17	0.21	0.06	0.67	0.18	0.17
logMAR	**−0.35**	**0.008**	**−0.41**	**0.002**	**−0.39**	**0.003**
cpRNFLT (μm)	**0.34**	**0.009**	**0.33**	**0.013**	**0.31**	**0.021**
Spherical equivalent (D)	0.09	0.50	0.08	0.54	0.09	0.50
preIOP (mmHg)	0.12	0.39	0.06	0.65	−0.02	0.91

The data (correlation coefficient value and *p* value) are described in each column.
Values in bold are statistically significant.

structure and function for threshold, TD, or PD (Figure 2G–I).

In this way, we established the correlation formula between macular OCT parameters and HFA 10-2 results for each test point. We then used the inverse calculation of the correlation formulas for each of the 68 test points to create an OCT parameter-derived simulation of the sensitivity of the visual field. We validated the simulated visual fields with an additive data set from the patients.

First, we compared the average simulated visual field sensitivity with real measured HFA 10-2 parameters (threshold, TD and PD) in the study group. There was a significant correlation between the averaged simulated visual fields and the real visual sensitivity mean, as shown in Table 3. The simulation produced from RNFLT data showed a significant correlation to the real average threshold ($r = 0.76$), TD ($r = 0.77$) and PD ($r = 0.31$). The simulation produced from GCC data showed a significant correlation to the real average threshold ($r = 0.72$) and TD ($r = 0.73$), but not to PD ($r = 0.12$). The simulation produced from GCL + IPL data showed a significant correlation to the real average threshold ($r = 0.56$) and TD ($r = 0.56$), but not to PD ($r = 0.08$).

Next, we validated the simulated visual fields with an additive data set of 29 other glaucoma patients. The demographic data for these patients are listed in Table 4. The average age of the patients was 65.7 ± 11.1 years, average spherical equivalent was -2.8 ± 2.2 diopters, average logMAR visual acuity was 0.084 ± 0.28, average HFA 30-2 MD was -12.1 ± 8.9 dB, average pretreated IOP was 18.3 ± 3.5 mmHg and average cpRNFLT was 79.3 ± 14.8 μm.

We were able to find a significant correlation between the average from the simulated visual fields and the real measured mean of visual fields parameters, as shown in Table 5. The simulation created from RNFLT data was also significantly correlated with real average threshold values ($r = 0.87$, $p < 0.001$), as well as TD ($r = 0.86$, $p < 0.001$) and PD values ($r = 0.64$, $p < 0.001$). The simulation created from GCC data showed a significant correlation to real average threshold values ($r = 0.78$, $p < 0.001$), as well as TD ($r = 0.77$, $p < 0.001$), but not to PD values ($r = 0.35$, $p = 0.067$). The GCL + IPL-derived simulation showed significant correlation to real average threshold values ($r = 0.63$, $p < 0.001$), as well as TD ($r = 0.62$, $p < 0.001$), but not PD values ($r = 0.22$, $p < 0.254$). We constructed a simulated grayscale visual field from RNFL with ten shades of gray representing 5 dB steps, as shown in Figure 3.

DISCUSSION

In this study, our results showed structure and function to be significantly correlated in the macular area. The correlation maps for RNFL, GCC and GCL + IPL had characteristic variations; the map for RNFL displayed a higher correlation coefficient with average visual sensitivity. We created a simulated visual field with an inverse calculation and the correlation formula for macular OCT thickness in each layer and the parameters from the HFA 10-2 program. We found that the simulation was significantly correlated with real results from the HFA 10-2 program. We therefore believe that simulated visual fields produced from OCT macular map data may have a real and valuable use in a routine clinical setting.

We found that the sensitivity of the macular visual field had a different correlation coefficient for each retinal layer. There was a higher correlation between HFA average threshold and RNFLT than thickness of GCC or GCL + IPL. Each layer of the retina contains a different section of the ganglion cells. The RNFL contains the axons and the GCL + IPL contains the cell bodies and dendrites, while the GCC contains all parts. Degeneration of the axons and dendrites has been detected in glaucoma patients.[14] After axons degenerate, microglia phagocyte the resulting debris and the thickness of the RNFL immediately decreases. These data suggest that axonal loss in RGCs may be better correlated to functional deterioration than it is to cell body loss in the macular area.

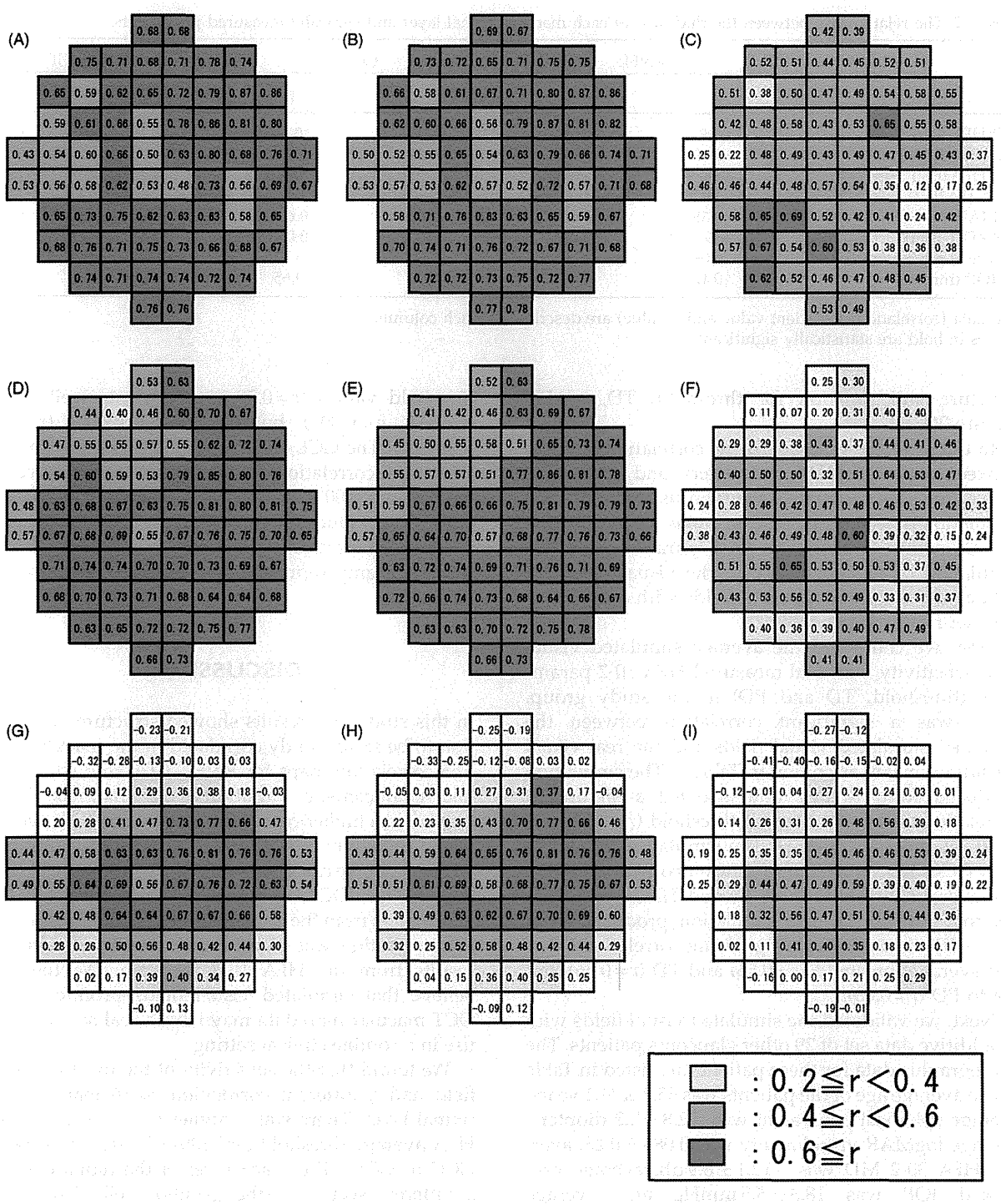

FIGURE 2 Distribution of the correlation coefficient for RNFLT, GCC, GCL + IPL and HFA 10-2 parameters in all 68 test points. Distribution grayscale maps showing the correlation coefficient for RNFLT (A–C), GCC (D–F) and GCL + IPL (G–I). Left panel (A, D, G) showed the threshold. Left side of figures was nasal side. Central panel (B, E, H) showed TD. Right panel (C, F, I) showed PD. Darker shades of gray indicate a higher correlation coefficient, with a step scale of 0.2. The white column indicates no statistical significance.

Our results showed a characteristic distribution of the correlation coefficient. The correlation between RNFLT and each HFA parameter in the overall nasal visual field was weaker than the correlation between the GCC and each HFA parameter in the upper nasal visual field. The nasal area is known to be a common site of glaucomatous visual field loss, and the threshold in this area can easily reach zero. OCT measurements of retinal layer thickness never reach zero, however, due to the presence of astrocytes and

TABLE 3 The relationship between VFs simulated from different macular maps and HFA 10-2 parameters.

	Calculated VF value					
	from RNFL		from GCC		from GCL+IPL	
	R	*p*	*r*	*p*	*r*	*p*
Measured mean of threshold	**0.76**	**<0.001**	**0.72**	**<0.001**	**0.56**	**<0.001**
Measured mean of TD	**0.77**	**<0.001**	**0.73**	**<0.001**	**0.56**	**<0.001**
Measured mean of PD	**0.31**	**0.016**	0.12	0.35	0.08	0.57

Values in bold are statistically significant.

TABLE 4 Demographic data for additive glaucoma patients used to validate the simulation.

Sex Male: Female, *n* (%)	16 (55%):13 (45%)
Age (yrs)	60.8 ± 9.0
Spherical equivalent (D)	−4.2 ± 2.9
Visual acuity (logMAR)	0.003 ± 0.11
MD of HFA30-2 (dB)	−17.2 ± 8.4
Pretreated IOP (mmHg)	18.3 ± 3.5
cpRNFLT (μm)	74.8 ± 13.7

TABLE 5 The relationship between HFA 10-2 parameters and simulated VFs produced from different macular maps.

	Calculated VF value					
	from RNFL		from GCC		from GCL+IPL	
	R	*p*	*r*	*p*	*r*	*p*
Measured mean of threshold	**0.87**	**<0.001**	**0.78**	**<0.001**	**0.63**	**<0.001**
Measured mean of TD	**0.86**	**<0.001**	**0.77**	**<0.001**	**0.62**	**<0.001**
Measured mean of PD	**0.64**	**<0.001**	0.35	0.07	0.22	0.25

Values in bold are statistically significant.

capillaries. Additionally, automatic segmentation of the retinal layers becomes difficult when the layers are very thin. In the nasal area, these factors combine to lower the value of the correlation coefficient between macular structure and function.

We used the inverse calculation with the correlation formula between RNFLT and the threshold to create simulated visual fields, and found that they were significantly correlated with real visual fields. Since it is important to assess the relationship between structure and function to adequately diagnose and manage glaucoma, visual field examinations must be included in routine tests for patients with visual field loss. In certain situations, however, speculation based on visual field simulations created from macular OCT maps may be worthwhile. In routine visual field tests, the HFA 24-2 or 30-2 programs are used more often than 10-2. It is usually inconvenient to perform examinations with the both 24-2 or 30-2 and 10-2 programs on the same day, due to the length of time required and the fatigue imposed on the patient. Visual field simulations may be especially helpful in examining patients with mental deterioration or dementia.

We acknowledge the limitations of this study. First, it comprised only a small number of glaucoma patients, and the nature of the study was retrospective. Second, the correlation between structure and function has been reported to be biased by age, axial length, stage of glaucoma and myopia.[15,16] To decrease the influence of these biases on the results, we excluded from the study patients with relatively high myopia (less than −8 diopter) and glaucoma, and used a single regression analysis to confirm that the spherical equivalent was not associated with any of the macular OCT map parameters from this study (Table 2). Third, although there was anatomical displacement of the RNFL,[17] GCC,[10] and GCL + IPL[18] in the fovea, we did not include it in our assessment of the structure and function relationship. Finally, assessment of the macula in glaucoma patients has a built-in selection bias, because in most cases, patients examined with the 10-2 HFA tend to have evidence of glaucomatous damage in the macula. The macula, however, is not always involved in the progress of glaucoma. In the future, a larger, multicenter study may be necessary.